Title

Age-dependent Lamin changes induce cardiac dysfunction via dysregulation of cardiac transcriptional programs

Journal

Nature Aging, 3(1)

ISSN

2662-8465

Authors

Kirkland, Natalie J

Skalak, Scott H

Whitehead, Alexander J

et al.

Publication Date

2023

DOI

10.1038/s43587-022-00323-8

Peer reviewed

nature aging

Article

https://doi.org/10.1038/s43587-022-00323-8

Age-dependent Lamin changes induce cardiac dysfunction via dysregulation of cardiac transcriptional programs

Received: 26 October 2021

Accepted: 31 October 2022

Published online: 22 December 2022

Check for updates

Natalie J. Kirkland[1,2], Scott H. Skalak[1,2], Alexander J. Whitehead[1,2], James D. Hocker[3,4], Pranjali Beri[1,2], Geo Vogler[5], Bill Hum[5], Mingyi Wang[6], Edward G. Lakatta[6], Bing Ren[3,4,7], Rolf Bodmer[5] & Adam J. Engler[1,2,4]

As we age, structural changes contribute to progressive decline in organ function, which in the heart act through poorly characterized mechanisms. Taking advantage of the short lifespan and conserved cardiac proteome of the fruit fly, we found that cardiomyocytes exhibit progressive loss of Lamin C (mammalian Lamin A/C homolog) with age, coincident with decreasing nuclear size and increasing nuclear stiffness. Premature genetic reduction of Lamin C phenocopies aging's effects on the nucleus and subsequently decreases heart contractility and sarcomere organization. Notably, Lamin C reduction downregulates myogenic transcription factors and cytoskeletal regulators, possibly via reduced chromatin accessibility. Subsequently, we find a role for cardiac transcription factors in regulating adult heart contractility and show that maintenance of Lamin C and cardiac transcription factor expression, prevents age-dependent cardiac decline. Our findings are conserved in aged nonhuman primates and mice, demonstrating that age-dependent nuclear remodeling is a major mechanism contributing to cardiac dysfunction.

With aging comes a progressive decline in organ function[1,2], but age-related decline in heart performance is especially critical as cardiovascular disease is the leading cause of mortality worldwide[3]. Aging results in the progressive loss of structural organization[4,5], which can limit contractility[1,6] and result in heart failure[7]. High prevalence of age-related cardiac dysfunction may in part be because cardiomyocyte (CM) renewal is limited[8] and therefore, maintenance of cardiac function over time must rely on compensatory mechanisms; these are multifaceted but are tightly linked to the integrity of key structural elements, for example, intercalated discs, sarcomeres and the extracellular matrix. Reducing force on CMs or compensating with transgenic overexpression of intercalated disc proteins can partially reverse heart dysfunction by restoring structural organization and gene expression[6,7]. As physical forces transduced to the nucleus can impact chromatin organization and induce changes in gene expression[9–11], nuclear changes may similarly be a mechanism contributing to age-associated cardiac dysfunction.

Structural changes in the nucleus are primarily governed by the nuclear lamina, an intermediate filament meshwork composed of A- and B-type Lamins. The lamina is tethered to the cytoskeleton[12,13] via the linker of the cytoskeleton (LINC) complex[9–11] as well as to chromatin[14,15] via lamina-associated domains (LADs)[16]. Along with the perinuclear cytoskeleton[12,13] and chromatin[14,15], the nuclear lamina regulates nuclear properties, including stiffness, size and shape[17–26]. In mechanically

[1]Department of Bioengineering, University California San Diego, La Jolla, CA, USA. [2]Sanford Consortium for Regenerative Medicine, La Jolla, CA, USA. [3]Cell and Molecular Medicine, University California San Diego, La Jolla, CA, USA. [4]Biomedical Sciences Program, University California San Diego, La Jolla, CA, USA. [5]Development, Aging and Regeneration Program, Sanford-Burnham-Prebys Medical Discovery Institute, La Jolla, CA, USA. [6]Laboratory of Cardiovascular Science, Intramural Research Program, National Institute on Aging, National Institutes of Health, Baltimore, MD, USA. [7]Ludwig Institute for Cancer Research, La Jolla, CA, USA. e-mail: aengler@ucsd.edu

active tissues, lamin mutations can give rise to muscular dystrophy[27,28] and cardiomyopathies[29], which also manifest in premature aging syndromes, for example, Hutchinson–Gilford progeria syndrome (HGPS)[30]. Lamin mutations cause dysmorphic nuclei, epigenetic dysregulation and DNA damage[31–34]; however, changes in nuclear shape, which are conserved from invertebrates[35,36] to humans[37], have been observed upon aging in the absence of lamin mutations. Age-related changes in nuclear shape also accompany loss of heterochromatin[37,38] and accumulation of DNA damage[37]. In some cases, progerin (truncated Lamin A; LamA) has been identified in aging skin[39] and dilated cardiomyopathy[40] in the absence of gene mutation. Furthermore, lamin expression decreases with age in some tissues[41–43], with loss of Lamin B (LamB), a well-known aging marker[42], and which may decrease CM regenerative capacity and increase ploidy[44]. LamA and Lamin C (LamC), two splice variants of the *lmna* gene) are the dominant adult cardiac Lamins and age-associated reduction has been observed in mouse CMs[41], but how lowered expression influences heart function and cardiac aging is unknown. Insights from LamA haploinsufficient mutant mice suggest that Lamin reduction is as detrimental to heart function as progerin mutants; mice develop dilated cardiomyopathy via loss of sarcomere-nuclear coupling, show defective nuclear transport and fail to activate compensatory hypertrophic pathways[45]. Thus, age-associated changes to nuclear shape and Lamin composition, herein referred to as nuclear remodeling, could be a major mechanism contributing to organ dysfunction, yet mechanisms contributing to age-dependent nuclear changes and how they affect tissue function remain elusive.

To investigate a role for age-dependent nuclear remodeling in regulating heart function, we primarily employ the invertebrate *Drosophila melanogaster*. *Drosophila* have a short lifespan, possess a simple tubular heart, which has a conserved cardiac proteome to humans[46] and importantly, undergo age-dependent cardiac decline[5,47]. We identified age-dependent remodeling unique to CM nuclei that is strongly influenced by an age-dependent reduction of LamC, the fly homolog to mammalian Lamin A/C. Genetic reduction of LamC in young flies phenocopies age-associated nuclear stiffening, decreases heart contractility and sarcomere disorganization and ultimately shortens lifespan. We show that LamC loss decreases expression of cardiomyocyte transcription factors, as well as cytoskeletal regulators, possibly by reducing their chromatin accessibility. Genetic reduction of CM transcription factors phenocopies age-dependent loss of heart function, while preserving their expression by expressing LamC or Hand exogenously delays cardiac decline. CM age-associated nuclear shrinkage is conserved from flies to nonhuman primates and therefore presents nuclear remodeling as a major mechanism contributing to age-related organ dysfunction.

Results

Cardiomyocyte nuclei remodel during aging

To understand whether age-associated nuclear remodeling influences heart function, we first sought to characterize how nuclear properties change upon aging in the *Drosophila* heart. Using two wild-type strains (w^{1118} and *yw*), we measured nuclear size and shape at 1, 3 and 5 weeks post-eclosure for surgically exposed hearts and specifically the A2–A3 region (Fig. 1a). Our high-throughput two-dimensional (2D) segmentation approach showed that common to both strains, CM nuclei decrease in cross-sectional area and become more circular upon aging (Fig. 1b and Extended Data Fig. 1a–c), which is contrary to observations in other cell types, for example, skeletal muscle nuclei[36] and fibroblasts[37]. To exclude that our observations were an artifact of our protocol, we segmented nuclei from the syncytial ventral muscle that overlays the CM pairs within the same confocal images (Fig. 1a). Here, we found that ventral muscle nuclei increase in size upon aging, suggesting the reduction in nuclear size is CM specific (Extended Data Fig. 1d). Nuclear atrophy is conserved in three dimensions, as we found that CM nuclear volume also decreases with age in w^{1118} flies (Fig. 1c and Extended Data Fig. 1e). As morphology and mechanics are often linked, we measured nuclear stiffness at 1 and 5 weeks of age using atomic force microscopy (AFM). CM nuclei, selected based on *Hand*-promoter-specific nuclear green fluorescent protein (GFP) expression and size (smaller than the pericardial nuclei), were more than twofold stiffer in aged flies (Fig. 1d). Together, our results show that CM nuclei become smaller, more circular and stiffer with age.

Cardiomyocyte Lamin RNA and protein decrease during aging

To identify candidate genes that may regulate age-associated nuclear structural changes, we performed bulk RNA sequencing (RNA-seq) on isolated *Drosophila* heart tubes (Fig. 2a and Supplementary Table 1). Approximately 1,494 differentially expressed genes (DEGs; $-1.25 >$ fold change (FC) > 1.25, (false discovery rate (FDR)-adjusted *P* value (P_{adj}) < 0.05) were identified and based on Gene Ontology (GO) analysis, represented terms primarily related to the cytoskeleton and sarcomere, extracellular matrix (ECM) and adhesion, and chromatin regulation and nuclear envelope (Fig. 2b and Supplementary Table 2). Many DEGs in this latter ontology (Extended Data Fig. 2a) are common to age-related terms, for example, DNA damage, repair and histone regulation (Extended Data Fig. 2b). Notably, several nuclear envelope genes were downregulated, including LamC, two homologs of nesprin, LINC complex proteins, Klarischt (Klar) and Msp300 (Fig. 2c). Utilizing RNA in situ with hybridization chain reaction (HCR)[48] to visualize messenger RNA transcripts and confirm transcriptome analyses specifically in CMs, we found that LamC mRNA expression indeed decreases upon aging as did LamB transcripts (Extended Data Fig. 2C,D) consistent with other aging systems[49]. Other cell types present in the heart may explain the absence of differential expression for LamB in bulk RNA-seq (Fig. 1a). Single nuclear RNA-seq performed as part of the Fly Cell Atlas[50] indicates that CMs may represent only 3.5% of the heart nuclei and thus is a caveat to our bulk RNA-seq approach. Subsequently, we verified via corrected total nuclear fluorescence (CTNF) that size-normalized expression of LamB and LamC decreased upon aging (Fig. 2d and Extended Data Fig. 2e); however, unlike in progeria and aged donor fibroblasts where Lamin A/C relocates from the nucleoplasm to the nuclear envelope[37], Lamins did not redistribute within aged nuclei (Extended Data Fig. 2e).

Lamin C reduction phenocopies age-related nuclear and cytoskeletal remodeling and shortens lifespan

Strong evidence from patients with laminopathies[23,37] suggests that Lamins regulate cell function and contribute to heart dysfunction[51]; however, evidence does not suggest what effects, if any, Lamins might have in aged hearts. Therefore, we sought to determine the effect of Lamin downregulation on CM function. We utilized $Hand^{4.2}$-*Gal4*, a heart (CMs and pericardial cells)-specific driver, to drive the expression of interfering RNA (RNAi) and verified cardiac-specific knockdown (KD) for LamB and LamC, relative to their background controls (*attp40* for *LamB* RNAi and *attp2* with Luciferase control RNAi for *LamC* RNAi; Fig. 3a and Extended Data Fig. 3A,B). To mark nuclei, we stained the Lamin isoform not targeted by RNAi and found that LamC and LamB reduction decreased nuclear area and perimeter compared to age-matched controls. Only *LamB* RNAi nuclei were more circular at 1 week than the *attp40* control (Fig. 3b and Extended Data Fig. 3C). By 4 weeks of adulthood, controls undergoing age-associated remodeling more closely mirrored RNAi effects observed at 1 week (Extended Data Fig. 3D). These distinct effects on nuclear morphology indicate that LamC and LamB may influence nuclear properties differently. Indeed, nuclei extracted from *LamC* RNAi hearts at 1 week were stiffer than age-matched controls and mimicked 4-week-old control nuclei, whereas *LamB* RNAi heart nuclei were softer than controls and did not phenocopy aging (Fig. 3c).

Along with nuclear stiffness, we found differential effects on heart function upon LamB or LamC reduction. Surgically exposed

https://doi.org/10.1038/s43587-022-00323-8

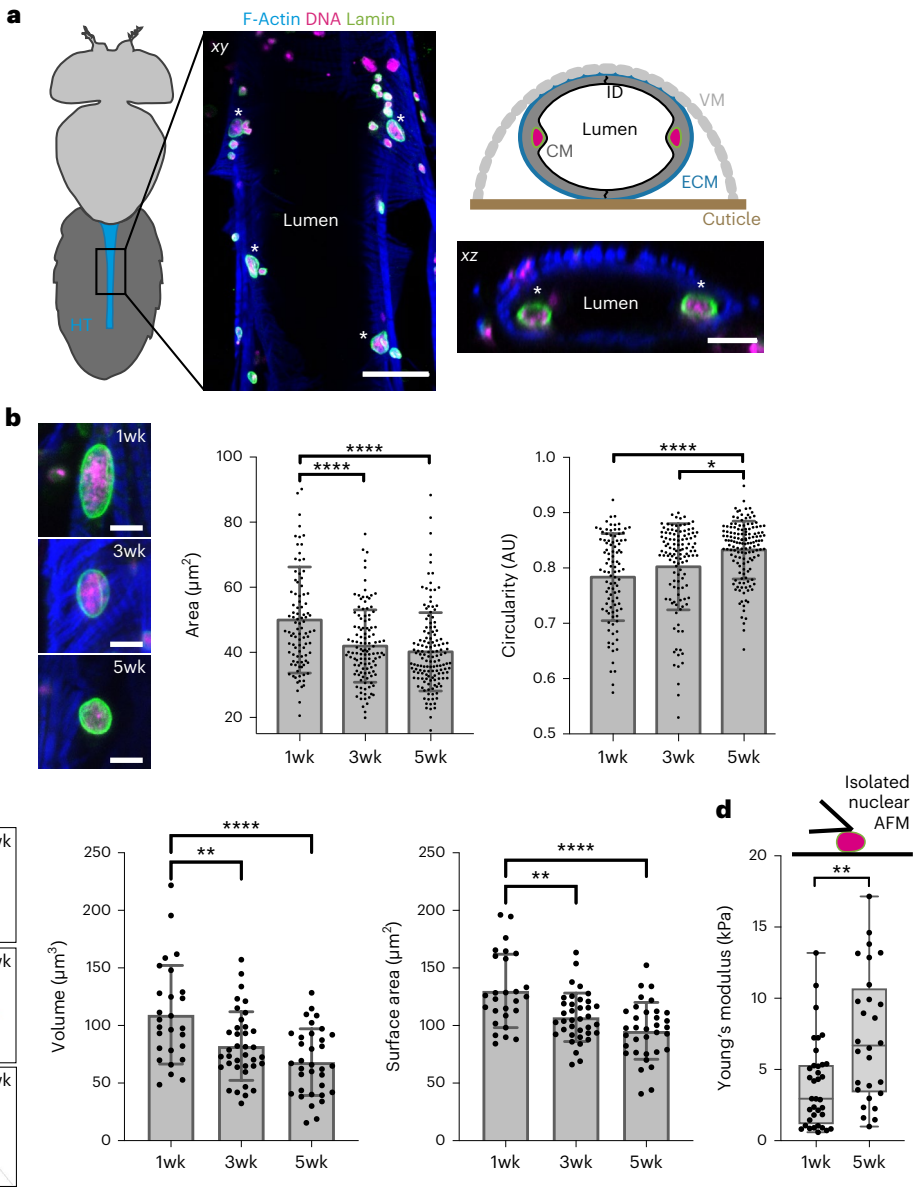

Fig. 1 | Age-associated changes in cardiac nuclear morphology and mechanics. a, Schematic of ventral *Drosophila* body plan with the heart tube in the abdomen highlighted in blue. Expanded view of the heart tube shows a coronal (*xy*) confocal section through the heart tube (center) as well as a transverse (*xz*) confocal section and schematic to highlight nuclear position in the luminal space (right). Asterisks indicate CM nuclei. Scale bar, 20 µm. **b**, Images of w^{1118} fly nuclei (left) and plot of their corresponding 2D projection data (right). Scale bar, 5 µm. $n = 96$, 116 and 141 nuclei for 1-, 3- and 5-week-old adults, respectively. Images were obtained from separate experimental imaging sessions and thus the brightness of the LamB staining was autoscaled to highlight nuclear edge and not to represent local protein concentration. **c**, 3D renderings of cardiac nuclei (left) and their corresponding for volume and surface area. $n = 27$, 37 and 34 nuclei for 1-, 3- and 5-week-old adult w^{1118} flies respectively. **d**, AFM nuclear indentation schematic (top) and plot of stiffness values (Young's modulus), for nuclei of w^{1118} flies (bottom). $n = 35$ and 28 nuclei for 1- and 5-week-old adults, respectively. $^{**}P < 10^{-2}$ and $^{****}P < 10^{-4}$ by one-way analysis of variance (ANOVA) with Tukey multiple comparisons test (**b**,**c**) and two-sided unpaired *t*-test with Welch's correction (**d**). Error bars (**b**,**c**) refer to mean ± s.d. and show min to max, with median and 25th and 75th interquartile range (**d**).

hearts from 1- and 4-week-old adults were subjected to live, high-speed imaging[52]. We observed that 1-week-old *LamC* RNAi hearts decreased in fractional shortening (Fig. 3d,e) (the difference of systolic and diastolic heart diameters divided by the diastolic diameter), relative to 1-week-old controls (Extended Data Fig. 3E,F) and were therefore less contractile. Conversely, *LamB* RNAi hearts only exhibited age-associated decreases in fractional shortening comparable to the *attp40* background control (Fig. 3d,e). As hearts with reduced LamC were less contractile, we examined how organized the sarcomeres (the contractile unit of CMs) were to assess whether organization might account for reduced fractional shortening. Using an automated, unbiased Fourier transform analytic[53], we found a significant decrease in CM sarcomere organization for 1-week-old *LamC* RNAi hearts relative to age-matched controls, which phenocopies the less organized 4-week-old control adult heart. Consistent with functional data, *LamB* RNAi hearts exhibited only age-associated reduction in sarcomere organization (Fig. 3f,g). As heart function is tightly linked to survival in *Drosophila*, we observed that only *LamC* RNAi flies had shortened lifespan (Fig. 3h), especially for adult flies of median age, compared to the background control. These results suggest that LamC loss during aging may contribute to heart dysfunction via sarcomere disorganization.

https://doi.org/10.1038/s43587-022-00323-8

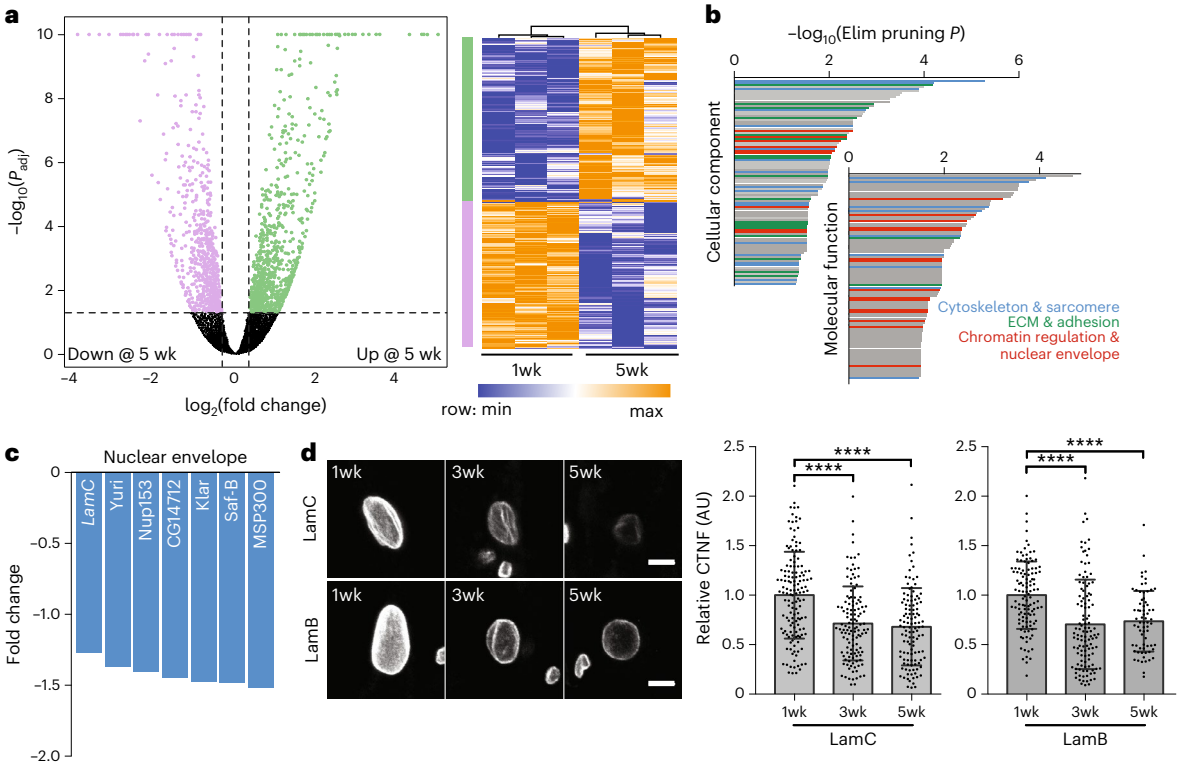

Fig. 2 | Natural aging downregulates nuclear envelope proteins. a, Volcano plot and heat map of bulk RNA-seq from surgically dissected heart tubes. FC represents 5-week-old w^{1118} fly hearts normalized to 1-week-old hearts and P_{adj} values were computed from quadruplicate repeats. A total of 1,494 DEGs were assessed from cutoffs of $-0.32 > \log_2(FC) > 0.3_2$ (or $-1.25 > FC > 1.25$) and $P_{adj} < 0.05$ (dashed lines) from comparisons of 15 fly hearts in quadruplicate biological replicates; DEGs increasing and decreasing with age are shown in green and purple, respectively. Heat maps are normalized within each gene/row. **b**, The top 100 molecular function and cellular component GO terms are plotted based on elimination pruning *P* value. Terms related to cytoskeleton and sarcomere, ECM and adhesion, and chromatin remodeling and nuclear envelope are annotated by color. **c**, Given as absolute FC, the expression of selected genes associated with nuclear envelope terms are plotted, with *LamC* expression noted with italics. **d**, Confocal projection images of CM nuclei showing *LamB* and *LamC* expression with age (left). Scale bar, 5 µm. CTNF (right), which adjusts for nucleus size, is plotted for *LamB* and *LamC* as a function of adult fly age. $n = 141, 124, 116, 114, 107$ and 69 nuclei per condition from left to right for LamC and LamB aged 1-, 3- or 5 weeks of adulthood, respectively. $^{****}P < 10^{-4}$ by one-way ANOVA with Tukey multiple comparisons test. Error bars refer to mean ± s.d.

Aging and Lamin C reduction alter chromatin accessibility at mesoderm transcription factor loci

While heart dysfunction may occur via sarcomere disorganization, the common upstream mechanism for *LamC* RNAi and natural aging are unknown. Given Lamin's role in anchoring chromatin and their link to cardiomyopathies[54], we hypothesized that cardiac dysfunction induced by Lamin deficits could be mediated by changes in chromatin organization. Assay for transposase-accessible chromatin sequencing[55] (ATAC-seq) was performed on isolated heart nuclei and we verified detection of accessibility peaks mapping to *Drosophila* heart-specific and enriched genes *Hand* and *tinman* (*tin*) and sarcomere genes *Tropomyosin* and *Mhc* (Fig. 4a). Subsequently, we compared differentially accessible regions (DARs) for 1- and 5-week-old wild-type (w^{1118}), 1-week-old *LamC* RNAi (versus *attp2* background control) and 1-week-old *LamB* RNAi (versus *attp40* background control) hearts ($-1.25 > FC > 1.25$, $P_{adj} < 0.1$). There were more DARs with aging compared to RNAi hearts (Fig. 4b and Supplementary Table 3), likely because aging impacts all cardiac-related cells, whereas the RNAi was expressed only in CMs, which are a subset of all cells present in the heart tube (Fig. 1a). Notably, with less LamC, hearts had more DARs that were less accessible versus more accessible, an imbalance also observed in aging hearts (67.5% less accessible and 55.9% more accessible DARs). Conversely, *LamB* RNAi had fewer DARs overall and fewer that were less accessible (38.0%). Thus, while nuclei get smaller and stiffer in aged and *LamC* RNAi hearts, there are also changes in chromatin accessibility.

These data could suggest that *LamC* reduction might have effects on specific chromatin domains during aging, thus we asked to what extent the same genes were affected in the same direction (more or less accessible) for both aging and 1-week-old *LamC* RNAi. Analysis of DARs common to both datasets indicated that 68% of DARs were co-regulated, with more than half of the common DARs being less accessible (Fig. 4c and Supplementary Table 4). Conversely, more than half of the DARs shared between *LamB* RNAi and aging were mutually more accessible. These results indicate that *LamC* and *LamB* may differentially contribute to age-associated changes, with *LamC* reduction conferring a decrease in accessibility associated with a decline in heart performance.

To better understand how mutual DARs might contribute to loss of function, we identified the ontological terms associated with the genes most proximal to the less accessible regions. Mutually less-accessible genes revealed terms for contractile fibers and cell cortex in addition to differentiation, development and morphogenesis (Fig. 4d and Supplementary Table 5). Notably, the most highly significant terms contributed genes including the Snail-type transcription factor Escargot and the heart-specific transcription factor Hand (Fig. 4e), which do not change in accessibility for *LamB* RNAi (Fig. 4f). Hand is required for invertebrate and vertebrate CM specification[56] and therefore may function beyond development to maintain cardiac programs. If reduced chromatin accessibility leads to protein loss upon aging, it is possible that downstream cardiac expression could be dysregulated.

https://doi.org/10.1038/s43587-022-00323-8

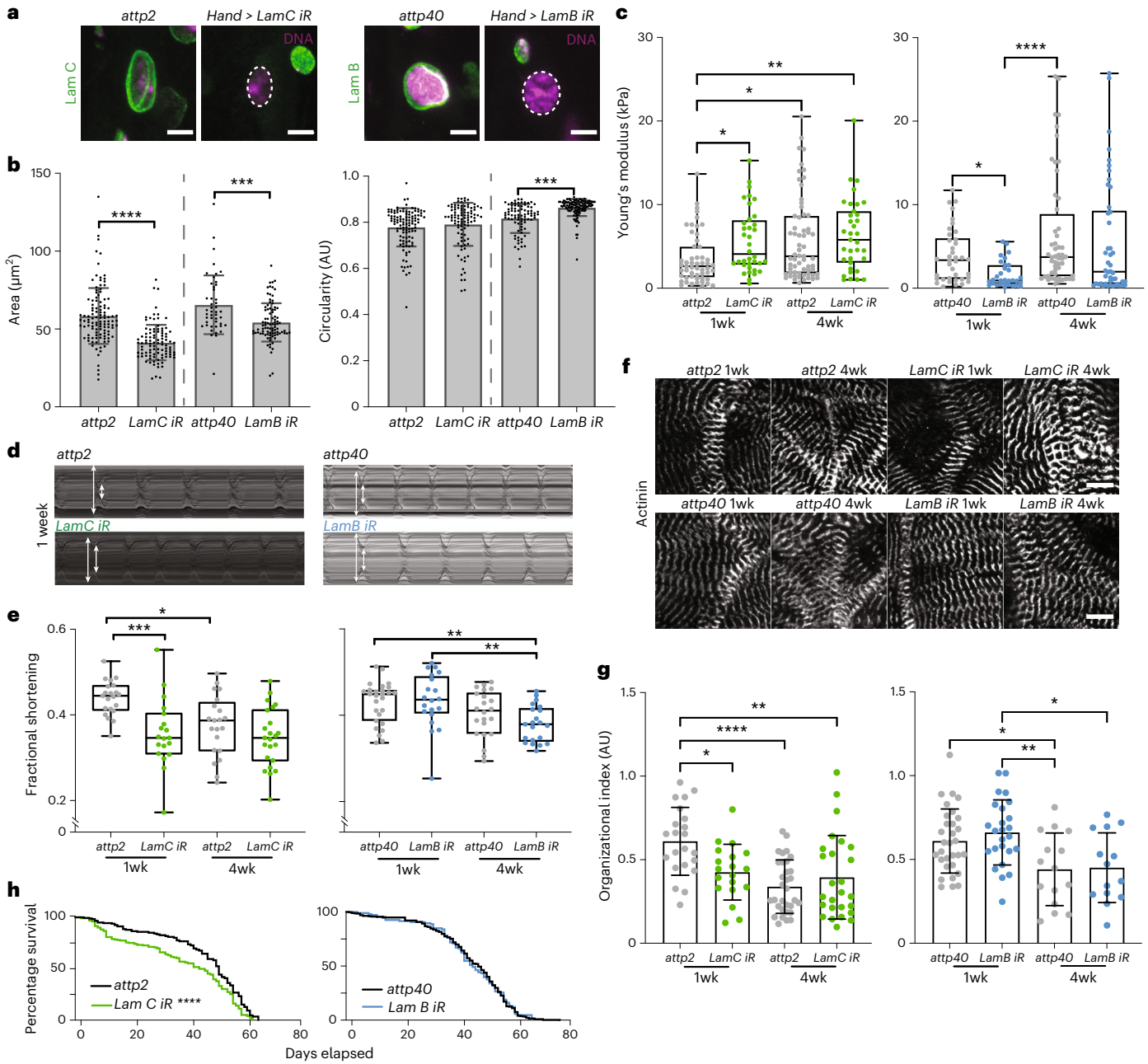

Fig. 3 | LamC, but not LamB, impacts cardiomyocyte aging, heart function and lifespan. a, Confocal cross-section images are shown for transgenic flies knocking down *LamB* and *LamC* by RNAi (iR; right) and their background fly line (left). Dashed lines indicate nuclear position based on DNA. Scale bar, 5 µm. **b**, Plots quantifying nuclear area (left) and circularity (right) based on confocal images of *LamB* and *LamC* RNAi lines and their genetic control background at 1 week of adulthood. $n = 111, 95, 46$ and 90 (hearts per condition; left to right). **c**, Plot of Young's modulus values is shown for nuclei of the indicated adult ages for *LamC* (green), *LamB* (blue) RNAi and their control strains (gray). $n = 53, 36, 63, 35, 38, 31, 52$ and 46 (hearts per condition; left to right). **d**, Representative kymographs of surgically exposed heart tubes for *LamC* (green), *LamB* (blue) RNAi and their control strains. White arrows mark the diastolic and systolic diameters. **e**, Fractional shortening at 1 and 4 weeks of adulthood is plotted for *LamC* (green) and *LamB* (blue) RNAi and their control strains. $n = 21, 18, 21, 23, 27, 20, 22$ and 20 (hearts per condition; left to right). **f**, Representative images of α-actinin staining for the indicated transgenic flies and their control backgrounds (paired by row) used to calculate organizational index in **g**. Scale bar, 10 µm. **g**, Organizational index is plotted for each heart tube. $n = 22, 19, 32, 26, 31, 25, 15$ and 14 (hearts per condition; left to right). **h**, Kaplan–Meier survival curve for *LamC* (green) and *LamB* (blue) RNAi and their control strains. 102, 148, 95 and 200 flies for attp2, *LamC* RNAi, *attp40* and *LamB* RNAi, respectively, were used in the plot. $^{*}P < 0.05$, $^{**}P < 10^{-2}$, $^{***}P < 10^{-3}$ and $^{****}P < 10^{-4}$ by one-way ANOVA with Tukey multiple comparisons test (**b**–**g**). $^{****}P < 10^{-4}$ based on log-rank (Mantel–Cox) test (**h**). Error bars refer to mean ± s.d. (**b**,**g**) and min to max, with median and 25th and 75th interquartile range (**c**,**e**).

Lamin C loss induces aging expression profile and represses cardiomyocyte transcription factors

To assess whether altered chromatin accessibility might lead to transcriptional dysregulation and if other cardiac-specific transcription factors were affected, we performed bulk RNA-seq for aged *attp2* background control and *LamC* RNAi hearts. We observed 344 DEGs resulting from heart-specific *LamC* loss at 1 week of age and 1,998 DEGs between 1- and 5-week-old *attp2* background flies (−1.25 > FC > 1.25, $P_{adj} < 0.05$; Fig. 5a and Supplementary Tables 6 and 7). When comparing the *attp2* and w^{1118} backgrounds, we found 688 common DEGs as a

https://doi.org/10.1038/s43587-022-00323-8

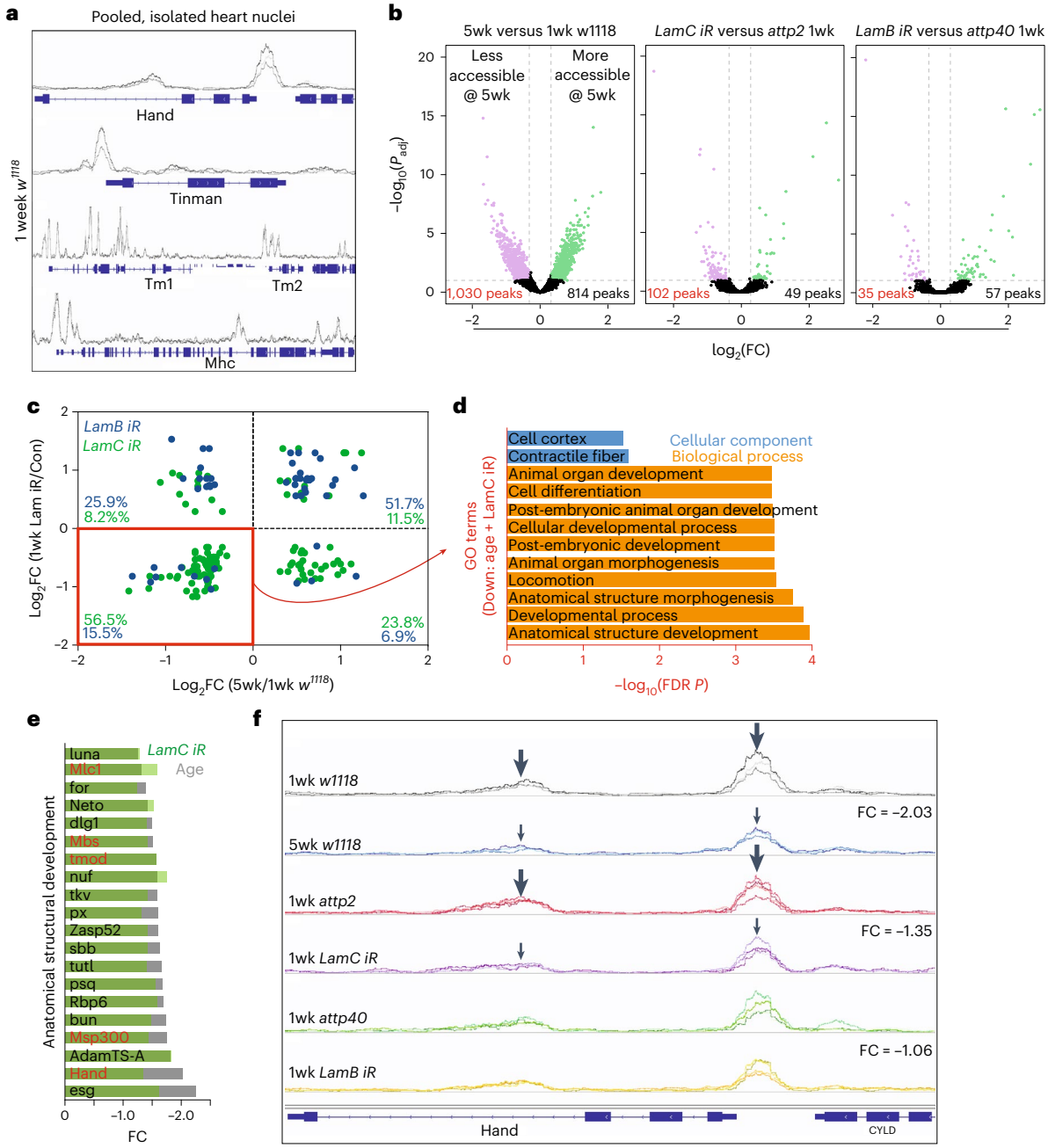

Fig. 4 | Chromatin accessibility decreases with age and *LamC* RNAi at sites of myogenic control. a, Map of accessibility peaks for *Drosophila* cardiac transcription factor genes *Hand* (top) and *tinman (tin;* top middle*)* and sarcomere genes *Tropomyosin* (*Tm1* and *Tm2*; bottom middle) and *Mhc* (bottom). Data are shown in triplicate sequencing runs using 1-week-old adult w^{1118} flies; three lines plotted in the panel for 50 pooled hearts per replicate. **b**, Volcano plots of the indicated aging or transgenic comparisons of DARs from ATAC-seq, assessed from $-0.32 > \log_2(FC) > 0.3_2$ (or $-1.25 > FC > 1.25$) and $P_{adj} < 0.05$. The number of peaks is annotated at the bottom for each comparison indicating if the region is more (black) or less (red) accessible relative to the comparator line. **c**, Scatter-plot is shown for ATAC-seq data comparing $\log_2(FC)$ in accessibility for genes based on effects from aging and *LamC* (green) or *LamB* (blue) RNAi. Percentages of data in each quadrant are shown. **d**, Top GO terms are plotted for co-downregulated peaks (closest associated gene) in aged and *LamC* RNAi fly comparisons and ordered based on the FDR-adjusted *P* value. **e**, Genes within the anatomical structure term were plotted for their fold change for aging (gray) and *LamC* RNAi (green). Genes names in red represent myogenic transcription factors or muscle-specific structure proteins. **f**, Map of accessibility peaks for the myogenic transcription factor *Hand*. Arrows indicate the location of a common DAR in *Hand* that is present and reduces in aged and *LamC* RNAi flies but not in *LamB* RNAi flies. Multiple lines per map indicate multiple sequencing runs of biological replicates. DAR fold change is annotated for each comparison.

function of age that either increased or decreased mutually (Extended Data Fig. 4A–C and Supplementary Table 8). We then identified mutually significant DEGs from *LamC* RNAi and aged hearts and observed that 110 DEGs of known function were present in both conditions (bottom left and top right quadrants; Fig. 5b and Supplementary Table 9). The common DEGs yield biological process GO terms related to aging (red; Fig. 5c and Supplementary Table 9), suggesting that LamC loss creates differential gene expression similar to natural aging. We also observed terms previously identified from ATAC-seq, including anatomical structure development and morphogenesis (blue; Fig. 5c), in which CM transcription factors *tin* and *H15* were downregulated (Fig. 5d). The imperfect overlap of the RNA and ATAC-seq may be accounted

for by differences in processing of heart tissue before isolation, for example RNA extraction was performed from intact hearts immersed in Quizol, whereas nuclei were first isolated by mechanical disruption and detergent-based lysis for ATAC-seq. HCR validated CM specificity of *tin*, *H15* and *Hand* (as found to be less accessible in ATAC-seq) and showed that all three were reduced upon aging and *LamC* RNAi (Fig. 5e,f). Conversely for *LamB* RNAi, hearts showed only an aging phenotype and no effect from the loss of LamB (Extended Data Fig. 4d,e). As the CM transcriptional network is highly conserved in mammals, and the potential importance of cardiac transcriptional changes on heart function, we focus our attention on Hand, Tin and H15 herein.

To confirm that LamC-dependent nuclear remodeling mediates the reduction of CM transcription factors rather than an off-target effect of the RNAi, we utilized heterozygous LamC null mutant flies[57]. We observed that LamC excision mutants, $LamC^{187}$ (375-bp deletion in the first exon) and $LamC^{296}$ (560-bp deletion in the first exon), reduce LamC expression and nuclear size compared to wild-type background controls (Extended Data Fig. 4F,G) and similarly to *LamC* RNAi (Fig. 3a,b). We identified a corresponding reduction in heart contractility compared to the background control, which for at least $LamC^{187}$ induced systolic dysfunction like heart-specific *LamC* RNAi (Extended Data Fig. 4H and Fig. 3d,e). Subsequently we confirmed that the CM transcription factors Tin, Hand and H15 were also downregulated in at least one heterozygous LamC mutant line (Extended Data Fig. 4I,J). Thus, we confirm a conserved LamC-dependent role in regulating CM transcription factor expression.

Our results thus far show that *LamC* loss occurs with age, makes nuclei smaller and stiffer, decreases CM transcription factor accessibility and expression and then disrupts sarcomeres to cause contractile dysfunction; however, our results do not yet establish whether loss of a myogenic program is critical for adult myocyte function.

Adult-onset myogenic transcription factor loss induces heart dysfunction, whereas maintaining Lamin C preserves heart function

The importance of myogenic transcription factors is highlighted by substantial sarcomere defects present when any one factor is silenced throughout development (Extended Data Fig. 5A; top). We therefore sought to assess whether CM transcription factor loss in adulthood, due to age-associated LamC loss, could also influence heart function. To approach this, we reared *Hand-Gal4* RNAi flies from the embryonic to pupal stages at 18 °C to lower the efficiency of the Gal4-UAS expression system[58] and then upon eclosure, the adult fly was transferred to 25 °C to induce strong expression while aging (Fig. 6a). In the case of CM transcription factor KD, the lowered efficiency of Gal4-UAS decreased the expression of RNAi to allow for structurally normal heart development (Extended Data Fig. 5A; bottom). We then assessed how RNAi in the adult fly influenced heart function; we observed a decrease in fractional shortening for *Hand* and *Tin* RNAi that proved similar to *LamC* RNAi. While *H15* RNAi did not yield a significant decrease, it indicated a trend toward decreased contractility (Fig. 6b and Extended Data Fig. 5B–G). In addition, we used a complementary method, employing the temperature-sensitive suppressor of Gal4, $TubGal80^{ts}$, with the heart-specific driver *Hand-Gal4* to assess the role of CM transcription factors in the adult heart. To suppress Gal4-UAS-driven expression during development, flies were reared at 18 °C, then at eclosure, 50% of adult flies were maintained at the permissive temperature (18 °C) or shifted to the non-permissive temperature (29 °C) at which denaturation of the Gal80 suppressor enables high-efficiency Gal4-UAS expression (Extended Data Fig. 5H). Live heart imaging showed that loss of each transcription factor in adults (2 weeks after temperature shift), still caused a significant decrease in fractional shortening compared to control backgrounds, which exhibited a slight but insignificant reduction in fractional shortening possibly due to relative differences in aging between flies maintained at each temperature, as higher temperatures accelerate aging (Extended Data Fig. 5i–m).

Conversely, we asked whether adult-onset *LamC* overexpression could preserve myogenic factor expression and function with age. Using the method described in Fig. 6a, we induced higher levels of exogenous LamC expression upon eclosure and aged flies up to 7 weeks at 25 °C. We observed that nuclear area was preserved despite aging when compared to the LacZ overexpression (OE) control; we note that LamC OE induced nuclear divisions and thus data represent total nuclear area per CM (Extended Data Fig. 6A,B). Subsequently, we found that sustained LamC expression up to 7 weeks, preserved fractional shortening and cardiac transcription factor expression compared to control (Fig. 6c–e). These observations were consistent with results using the alternative $tubGal80^{ts}$ temperature-sensitive induction system (Extended Data Fig. 6E–O). Finally, we asked whether overexpression of a single CM transcription factor was sufficient to preserve heart function upon aging and to mimic the influence of preserved LamC using the 18 °C to 25 °C method (Fig. 6a). We found that Hand OE generated viable adult flies, preserved heart contractility up to 7 weeks compared to controls and led to elevated expression of Hand, Tin and H15 transcription factors compared to controls at least to 4 weeks of age, suggesting a degree of co-regulation (Fig. 6f,g and Extended Data Fig. 6C,D). Together, our results establish that adult loss of myogenic programs is mediated by age-associated *LamC* loss, which may modulate their chromatin accessibility and subsequently reduces adult CM function (Fig. 7a).

Nuclear remodeling and myogenic transcription factor loss is conserved in mice and nonhuman primates

Despite physiological differences between tubular and chambered hearts, there is noteworthy overlap between the *Drosophila* and human cardiac proteomes[46]. We therefore sought to assess whether similar structural and transcriptional changes are conserved from the fly heart to the mammalian heart[41]. We observed in both mouse and monkey heart sections that nuclear size decreased and circularity increased upon aging, as we found in the fly heart tube (Fig. 7b,c).

Fig. 5 | LamC loss transcriptionally regulates myogenic transcription factors. **a**, Volcano plot and heat map of bulk RNA-seq from surgically dissected heart tubes from *LamC* RNAi flies compared to *attp2* control background flies at 1 week of age. The 344 DEGs were assessed from cutoffs of $-0.32 > \log_2 FC > 0.3_2$ (or $-1.25 > FC > 1.25$) and $P_{adj} < 0.05$ (dashed lines) from comparisons of 15 fly hearts in quadruplicate biological replicates; DEGs increasing and decreasing with *LamC* RNAi are shown in green and purple, respectively. Heat maps are normalized within each gene/row. **b**, Scatter-plot comparing $\log_2 FC$ from aging (1 and 5 weeks of age) and *LamC* RNAi compared to control background (*attp2*). Number of DEGs represent genes of known function. Data were categorized based on the cellular component GO term most closely matched. Distance from the red dashed line of unity was used identify co-regulated genes whose biological process GO terms were annotated and ordered based on their FDR *P* value (**c**). **d**, Genes within the anatomical structure term were plotted for their fold change for aging (gray) and *LamC* RNAi (green). Genes names in red represent myogenic transcription factors or muscle-specific structure proteins. **e**,**f**, Representative images of in situ HCF for transcription factors *H15*, *Hand* and *tin*, co-stained with 4,6-diamidino-2-phenylindole (DAPI), for *LamC* RNAi and control *attp2* flies at 1 and 4 weeks of adulthood (**e**) with quantification for each transcription factor (**f**) also shown (right) and quantification of the per cell percent area covered by each transcript. For *H15*, $n = 39, 76, 64$ and 45 cells for 1-week-old control, 1-week-old *LamC RNAi*, 4-week-old control and 4-week-old *LamC* RNAi, respectively. For *Hand*, $n = 71, 84, 52$ and 43 cells for 1-week-old control, 1-week-old *LamC* RNAi, 4-week-old control and 4-week-old *LamC* RNAi, respectively. For *tin*, $n = 69$, 101, 103 and 85 cells for 1-week-old control, 1-week-old *LamC* RNAi, 4-week-old control and 4-week-old *LamC* RNAi, respectively. $^*P < 0.05$, $^{**}P < 10^{-2}$, $^{***}P < 10^{-3}$ and $^{****}P < 10^{-4}$ by one-way ANOVA with Tukey multiple comparisons test. Bars (**f**) represent min to max, with median and 25th and 75th interquartile range.

https://doi.org/10.1038/s43587-022-00323-8

Furthermore, immunofluorescence staining of the mouse heart sections confirmed reduction of Lamin A/C (Fig. 7b), consistent with that seen in *Drosophila*. Subsequently, we found that mammalian homologs of fly transcription factors *Hand1*, *Nkx2.5* (homolog of *tin*) and *Tbx20* (homolog of *H15*) significantly decreased expression in aging mice hearts (Fig. 7d and Extended Data Fig. 7A,B) and that *Hand1*, *Hand2* and *Nkx2.5* significantly decreased in expression in aging nonhuman primate rhesus macaque hearts (Fig. 7e and Extended Data Fig. 7C,D), when normalized to at least one of three different, stable housekeeping genes. These data suggest that the functional decline attributed to CM transcription factor loss in flies could be a conserved mechanism, caused in part by physical remodeling of the nucleus.

Discussion

The role that nuclear remodeling has on heart function during natural aging has thus far been largely unexplored. Here, we demonstrate that CM nuclear remodeling (age-related loss of nuclear lamins), is intimately linked with tissue-level dysfunction. Genetically inducing

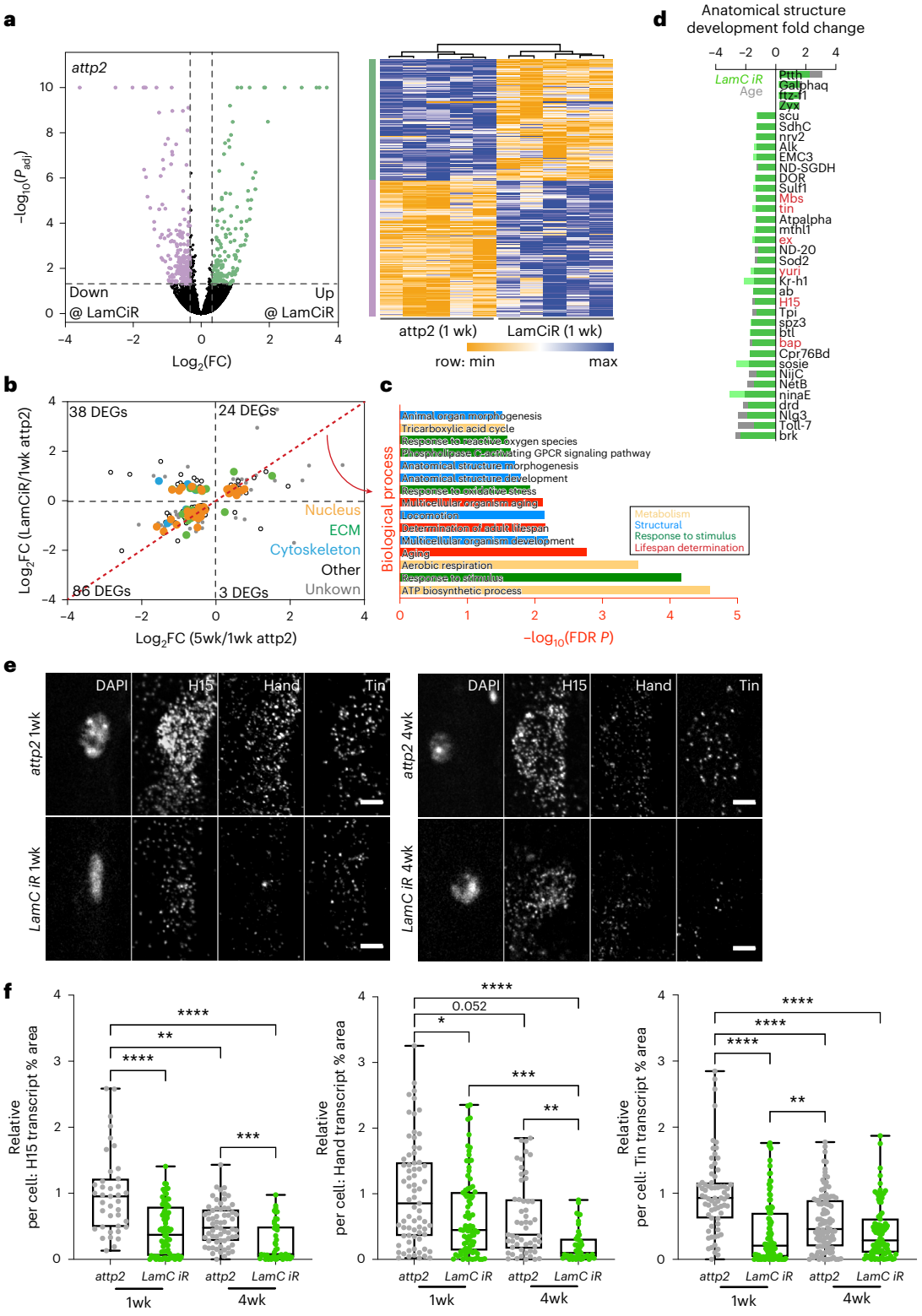

https://doi.org/10.1038/s43587-022-00323-8

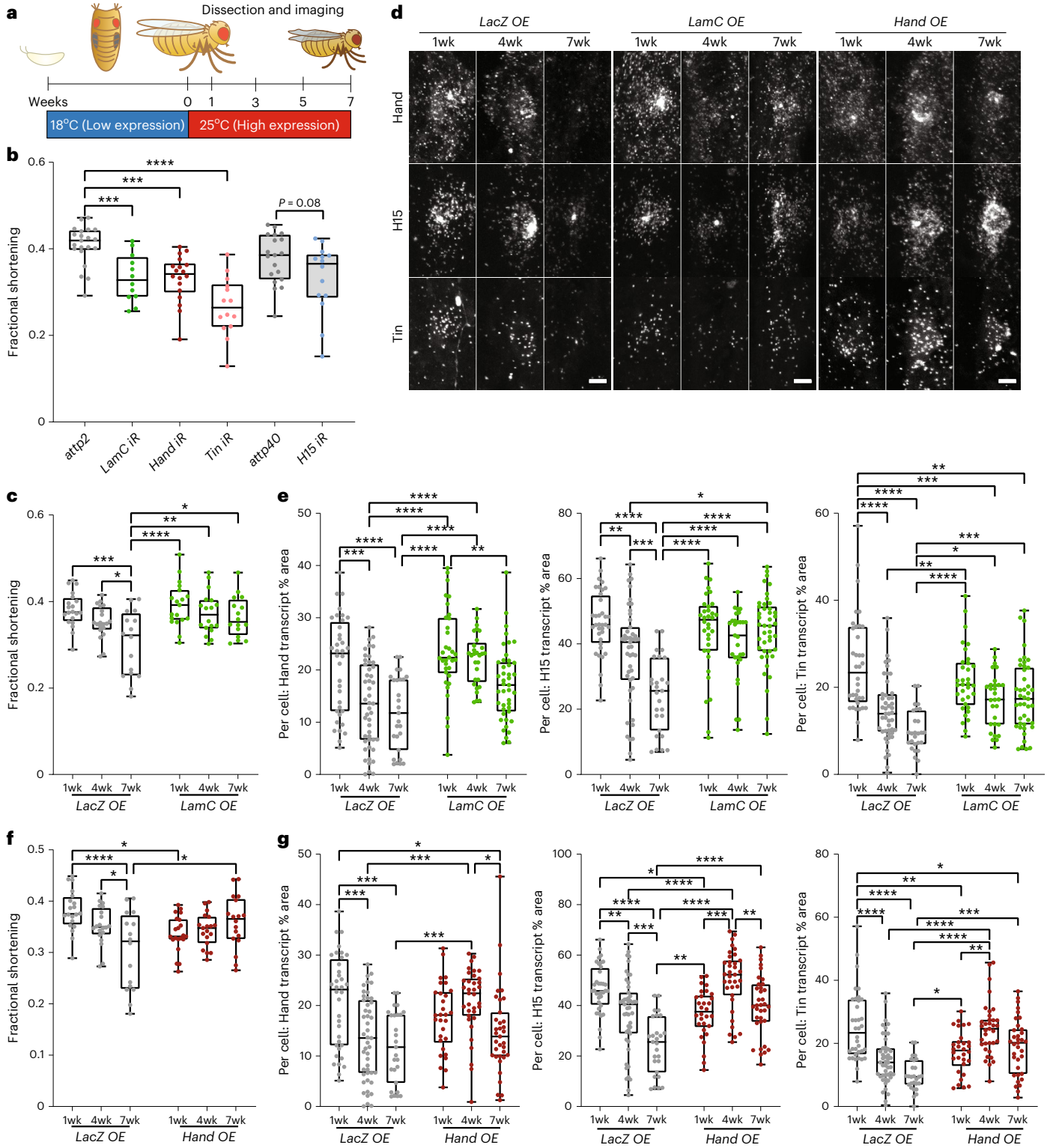

Fig. 6 | Myogenic transcription factors maintain heart contractility in aged flies. a, Schematic of temperature-sensitive transgenic expression where 18 °C minimizes Gal4-mediated expression up to adult fly eclosure. At 25 °C transgene expression is high enabling assessment of gene role in adult heart. **b**, Quantification of fractional shortening for surgically exposed hearts with *Hand-Gal4* driving expression of *LamC* RNAi (green), *Hand* RNAi (red), *Tin* RNAi (pink) and respective control *attp2* (gray) and *H15* RNAi (blue) with *attp40* control (gray) with temperature schedule shown in **a**; $n = 10, 12, 18, 15, 19$ and 14 (heart tubes left to right). **c**, Fractional shortening plots for *Hand-Gal4*-driven *LamC* overexpression (OE) by the regime shown in **a** with control, OE of LacZ; $n = 20, 20, 16, 19, 18, 16$ (heart tubes per age, left to right). **d**, Representative images of RNA in situ with HCF for Hand, H15 and Tin transcripts, with corresponding quantification of the per cell, percentage area for each transcript, for *LacZ* control and *LamC* OE in **e** and Hand OE in **g** each at 1, 4 and 7 weeks at 25 °C. Scale bar, 5 µm. **e**, $n = 36, 47, 27, 34, 29, 43$ (CM nuclei per genotype per age, left to right). **f**, Fractional shortening plots for *Hand-Gal4*-driven expression of *Hand* OE by the regime shown in **a** with control, OE of LacZ; $n = 20, 20, 16, 21, 19, 18$ (heart tubes per age, left to right). **g**, $n = 36, 47, 27, 30, 35, 35$ (note, same control; CM nuclei per age, left to right). $^{*}P < 0.05$, $^{**}P < 10^{-2}$, $^{***}P < 10^{-3}$ and $^{****}P < 10^{-4}$ by one-way ANOVA with Kruskal–Wallis test and Dunn's comparisons test (**b**) and two-way ANOVA with Sidak's multiple comparisons test. In all graphs, bars represent min to max, with median and 25th and 75th interquartile range.

https://doi.org/10.1038/s43587-022-00323-8

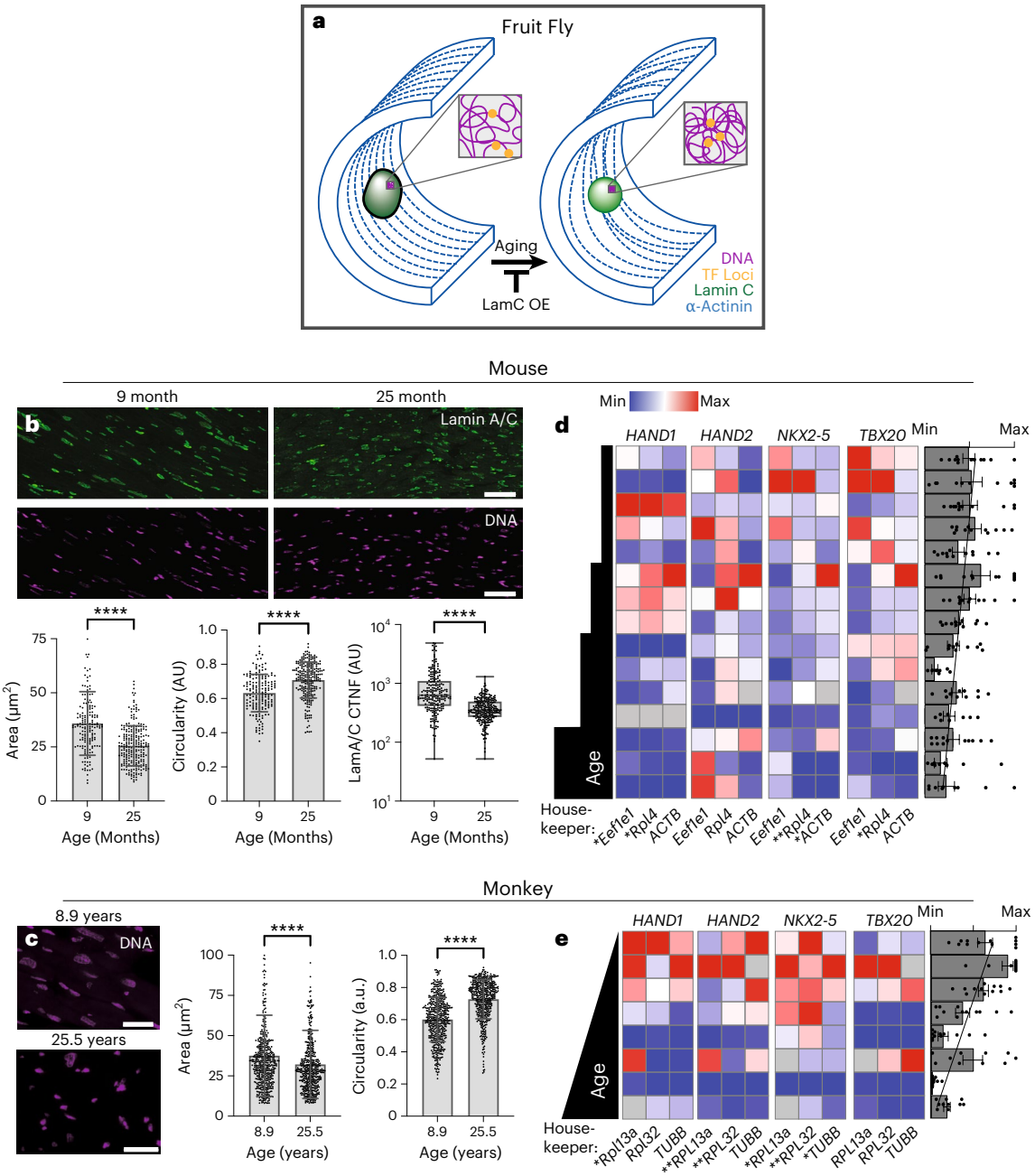

Fig. 7 | Nuclear remodeling induces adult-onset transcription factor loss, a process conserved in mice and nonhuman primates. a, Schematic depicting how age-associated, cardiac-specific reduction of nuclear lamins reduces nuclear volume and chromatin accessibility, especially for myogenic transcription factors. With less muscle transcription from key cardiac loci, sarcomeres become disordered with age and heart function is reduced. Lamin OE can overcome age-associate reduction and preserve function. **b**, Immunofluorescent staining of mouse heart sections at 9 and 29 months of age with anti-LamA/LamC (green) and DAPI (magenta). Scale bar, 30 μm. Below shows plots of projected nuclear area and circularity with respective ages; $n = 3$ biological replicates and three technical replicates. **c**, Immunofluorescent staining of monkey left ventricle sections at 8.9 and 25.5 years of age with anti-LamA/LamC (green) and DAPI (magenta). Scale bar, 30 μm. Plots of projected nuclear area and circularity with respective ages (bottom); $n = 3$ biological replicates and three technical replicates. **d**,**e**, qPCR results are plotted for mouse (**d**) and rhesus macaque (**e**) for the myogenic transcription factors Hand1, Hand2, Nkx2-5 and TBX20 as normalized by housekeepers Eef1e1, Rpl4 and ACTB for mouse and Rpl13a, Rpl20 and TUBB2 for macaque. Data were normalized to maximum and minimum expression within each gene and housekeeper for heat map. Bar graph and regression indicate the mean expression and s.e.m. across all genes and housekeepers for each animal; $r^2 = 0.50$ and 0.71 for mouse and macaque, respectively. $^*P < 0.05$, $^{**}P < 10^{-2}$, $^{***}P < 10^{-3}$ and $^{****}P < 10^{-4}$ by two-sided unpaired *t*-test (**b**,**c**, circularity) and with Welch's correction in (**b**,**c**, nuclear area). Significance in **d** and **e** indicate deviation from 0 for simple linear regression. Error bars (**b**, left and center, **c**) refer to mean ± s.d. and min to max, with median and 25th and 75th interquartile range (**b**, right).

nuclear remodeling leads to reduction in heart contractility, sarcomere disorganization and shortens lifespan by mimicking transcriptional changes that occur in natural aging. Our findings suggest that transcriptional misregulation downstream of nuclear remodeling may occur due to altered chromatin accessibility and notably, this represses CM fate transcription factors and sarcomeric structural components. We show that preserving 'youthful' nuclear properties such as high Lamin expression and nuclear morphology, maintains CM transcription factor

expression and heart function. These changes are conserved in both mice and nonhuman primates demonstrating nuclear remodeling and myogenic transcriptional programs as potential therapeutic targets for preserving heart function during aging.

Our observations of age-associated nuclear remodeling in *Drosophila*, mouse and nonhuman primate CMs are in contrast to existing observations in *Caenorhabditis elegans* intestinal cells[35], *Drosophila* skeletal muscle[36], aged human fibroblasts[37] and what is currently understood for progeria-related laminopathies[19,23,33,37]. Rather than increasing in size and dysmorphia, we observe that aging CM nuclei atrophy and become rounder, although more recent findings also indicate tissue-specific nuclear remodeling in *C. elegans*[59,60]. We demonstrate that CM nuclei stiffen upon aging in situ, an observation only seen previously in cell culture for progeria cells after multiple rounds of passaging[19]. Further supported by our assessment of non-CM ventral muscle nuclei that hypertrophy with age within the heart tube, our findings suggest that CMs have specific mechanisms mediating nuclear remodeling.

In the context of *Drosophila* CMs, we sought to understand how nuclear remodeling occurred upon aging and identified that nuclear lamins, LamC and LamB, in addition to nesprin-related proteins Klar and Msp300, were downregulated upon aging. Consistent with our data, Lamin B has been previously reported to be downregulated with age[43,49,61] possibly due to its role in senesence[42], whereas a functional role for age-associated Lamin A/C reduction has not previously been explored. We found that genetically reducing LamC prematurely was sufficient to induce aging-like nuclear atrophy, but conversely, overexpression was required to change nuclear size in Xenopus and HeLa[25]. While A and B-type Lamins differentially contribute to nuclear mechanics[20], we observed that reduction of A-type LamC increased CM nuclear stiffness despite softening of cultured cell nuclei with reduced Lamin A/C expression[20,26]. These differences could be accounted for by several hypotheses. First, *Drosophila* LamB and LamC could have differing functions compared to mammalian counterparts, although in other cell types, there is conservation between *Drosophila* and human Lamins[62]. Second, it is increasingly apparent that nuclei respond differently in 2D and three-dimensional (3D) environments. In 2D cell culture, nuclear wrinkling indicates membrane laxity, whereas in 3D environments[63,64], wrinkling is dependent on actin filaments intrusion into the perinuclear space and wrinkling infers high membrane tension[63]. Third, cell- or developmental-specific differences may result in alternative mechanics upon Lamin depletion. For example, Jevtic et al. show that in differentiated Xenopus cells, very high levels of Lamins can in fact decrease nuclear size[25]. Fourth, cell-specific LADs at the nuclear periphery show unique phenotypes with Lamin A/C mutations in human induced pluripotent stem cell-derived CMs versus adipocytes and hepatocytes[65]. Thus, differential Lamin–chromatin interactions could similarly contribute to altered mechanical regulation in aging cardiomyocytes versus other cell types.

Given the linkage of nuclear lamina to sarcomeres via the LINC complex, and chromatin via LADs[16], as well as the functional deficits we uncovered, our data provide confirmation of a role for A-type Lamins in age-dependent regulation of heart function. Removal of Lamins disrupts chromatin attachment to the nuclear periphery, higher-order chromatin organization and can influence gene expression[66–70]. These studies focus predominantly on stem cell fate and maturation, yet our data now suggest differences in post-mitotic tissues. We identified that in both aging and LamC reduction, differentially accessible peaks were skewed toward decreased accessibility, despite evidence that heterochromatin is lost in Lamin A/C mutants and with aging[23,31]. Correspondingly, studies specifically disrupting LADs yield conflicting results depending on cell origin; Chang et al. reported chromatin decompaction and redistribution in breast cancer cells[70], whereas Ulianov et al. found that topological-associated domains decondensed but global chromatin density increased in embryonic-derived *Drosophila* S2 cells[68]. Similarly, maintaining lamina but disrupting chromatin attachment increased chromatin compaction in *C. elegans* embryos[69]. Disrupting LADs can also show localized alterations in accessibility, with recent work demonstrating LamB loss leads to repositioning of disease-causing loci away from the nuclear periphery in post-mitotic neurones[71] and alters repressive H3K9me3 marks in *C. elegans*[72]. Two available datasets analyzing B-type LADs in *Drosophila*[73,74] identified 327 LADs in protein-coding regions, 40% of which corresponded to peaks in our dataset; however, less than 4% of the LADs were differentially regulated with LamC RNAi and and <2% changed with LamB RNAi, suggesting an LAD-independent aging mechanism. These conflicting examples, along with our data, suggest that accessibility both globally and locally for specific loci, could be context specific and our data propose that in the context of aging, reduced accessibility is coupled to dysfunction.

We show that ultimately, Lamin-mediated nuclear remodeling is a conserved process in vertebrates that reduces the expression of CM transcription factors, for example, Hand/HAND1/2, Tin/NKX2-5 and H15/Tbx20. We observe that specifically Hand is less accessible with aging and LamC reduction. In *Drosophila*, the highly conserved Tin transcription factor is an early initiator of cardiogenesis and binds between Hand exons 3 and 4 (ref. [75]), an intron that we observe to have reduced accessibility upon LamC reduction (Fig. 4f). Thus, reduced gene accessibility could further downregulate Hand and downstream myogenic transcription. We predict that reduced chromatin accessibility might also account for the reduction of Tin/NKX2-5 and H15/Tbx20 with age across flies, mice and monkeys. Our findings provide a Lamin-mediated interpretation for previous observations of reduced NKX2-5 in aged, isolated mouse CMs[76] and provides them with a role beyond development. We show in *Drosophila* that their adult-specific reduction gives rise to a marked reduction in heart function, supported by studies that find an adult-specific role for TBX20 when deleted in mice[77–79]. Consistent with these observations, CM transcription factors are misregulated in remodeling events leading to heart failure[80], for example, HAND is downregulated in rodent hypertrophy[81] and in human cardiomyopathy[82]. Furthermore, senescent myoblasts in aged skeletal muscle, exhibit altered myogenic transcription factors and result in smaller myotubes[83,84]. Together, Lamin-mediated misregulation of myogenic transcriptional programs likely has a major impact on mediating heart dysfunction during aging and may precede the development of heart failure. As preserving LamC maintained CM transcription factor expression and heart function despite aging in flies, and heart function was also preserved with adult Hand expression, our findings suggest that nuclear lamina remodeling is upstream of myogenic transcription regulation and a mechanism contributing to age-related organ dysfunction. These findings present several avenues for investigating therapeutic interventions to increase healthspan into advanced age.

Methods

Drosophila melanogaster

Fly stocks were raised in non-crowded conditions on standard fly food medium consisting of yeast, cornstarch and molasses (10% yeast, 12% sugar and 1.5% agar). Flies were raised at 25 °C except for the temperature-sensitive fly crosses (Hand-Gal4 crosses in Fig. 6 and Hand-Gal4, TubGal80ts; TubGal80ts; crosses in Extended Data Figs. 5 and 6), which were raised at 18 °C until eclosure, then transferred to 25 °C (Fig. 6) or 18 °C and 29 °C (Extended Data Figs. 5 and 6), respectively. Freshly eclosed flies were collected and aged such that day of collection was day 1. Flies were transferred to fresh food every 2–3 d. Female flies were used for subsequent heart analysis to ensure consistent heart morphology. The following fly lines were used from the Bloomington stock center: *white-1118* (w^{1118}), *yellow-white* (*yw*), *attp2; UAS-Luciferase* (31603), *UAS-LamC-RNAi* (31621), *attp40* (36304), *UAS-LamB-RNAi* (57501), *UAS-Stinger*-GFP (84277), *UAS-tinman-RNAi* (50663), *UAS-H15-RNAi* (57415), *UAS-Hand-RNAi* (28977). $Hand^{4.2}Gal4$ was acquired from

Olsen Laboratory[75] and modified by the Bodmer laboratory to make *Hand*$^{4.2}$*Gal4, TubGal80*^{ts}*; TubGal80*^{ts}. *UAS-LamC*, *Lamc*^{187} *and LamC*^{296} were gifted by the Walrath laboratory.

Mouse

All mouse experiments were performed in according to the guidelines established by the Institutional Animal Care and Use Committee (IACUC) at the University of California San Diego. Use of aged C57BL/6 mice was approved by the University of California San Diego IACUC under study no. S08172. All animals were provided with food and water ad libitum until the specific age time point at which point animals were killed by asphyxiation followed by cervical dislocation. The lower section of the left ventricle was removed from five young (5 months old), three juvenile (9 months old), four adult (14 months old) and three aged (24 months old) mice and snap-frozen in liquid nitrogen immediately after resection and stored at −80 °C. The remainder of the heart was washed in phosphate-buffered saline (PBS) before embedding in OCT for cryosectioning. OCT boats containing hearts were frozen on dry ice with methyl butane before storage at −80 °C.

Rhesus macaque

Ten adult male rhesus monkeys (8.87, 9.7, 10.66, 12.88, 14.12, 18.81, 19.59, 23.39, 24.73 and 25.48 years of age) were maintained at the National Institute on Aging (NIA) in accordance with National Institutes of Health (NIH) IACUC protocol AG000238-07 (Effects of Aging on Experimental Atherosclerosis in Nonhuman Primates). Left ventricular samples from macaque were flash-frozen for qPCR analysis or were formalin-fixed and paraffin-embedded and subsequently sectioned for immunofluorescence analysis.

Fly heart dissection

Flies were anesthetized with FlyNap (Carolina Biological Supply) and dissected in artificial hemolymph that was oxygenated using aerators as previously described[52].

Immunofluorescence and imaging

Hearts dissected in oxygenated artificial hemolymph were relaxed using 10 mM EGTA in oxygenated artificial hemolymph and immediately fixed with 4% formaldehyde in the same EGTA hemolymph solution for 20 min. The hearts were then rinsed 3× with PBS and washed for 3 × 10 min with 0.5% Triton 100-X in PBS (PBST). The hearts were then blocked with 1% BSA in PBST (PBST-BSA) for 30 min. Primary antibodies were prepared as indicated below in PBST-BSA and incubated overnight at 4 °C. PBST and PBST-BSA washes were repeated and secondary antibodies with DAPI and phalloidin were prepared in PBST-BSA and incubated for 1.5–2 h at room temperature. Following secondary incubation, hearts were washed for 3 × 20 min with PBST and then rinsed 3× with PBS to remove detergent. Antibodies and dyes used were mouse anti-LamC (DSHB, LC28.26), 1:500 dilution; mouse anti-LamB, 1:100 dilution (DSHB, ADL195); mouse anti-actinin (DSHB, 2G3-3D7) 1:100 dilution; DAPI (Sigma), 1:500 dilution; rhodamine-phalloidin (Thermo Fisher, R415), 1:250 dilution and donkey anti-mouse Alexa Fluor 488 (Thermo Fisher, A21202), 1:500 dilution.

For imaging, the cuticle around the hearts was subsequently trimmed down to a small rectangle to prevent obstruction of the heart, then hearts were transferred to Fluormount G slide-mounting medium for antibody-based imaging or ProLong Glass Mountant (Invitrogen) for HCR imaging. The A2–A3 region of the heart was imaged on a Zeiss LSM780 inverted confocal microscope with a ×40 objective, 1× zoom, 0.44-µm depth resolution for nuclear imaging or 0.88 µm for actinin and HCR imaging and at a resolution of 2,148 × 1,076 *xy* pixels.

Mouse heart sections embedded in OCT were cryosectioned and stored at −80 °C before fixation and staining. Slides were directly fixed with 4% PFA in PBS for 20 min at −20 °C with regular agitation to prevent freezing. Slides were subsequently washed 3 × 5 min with PBS and permeabilized for 1 h with 1% PBS-Triton 100-X. Primary antibody was prepared in 10% fetal bovine serum (FBS) with PBS (anti-Lamin A/C 1:250 dilution, Cell Signaling Technology, 4C11) and incubated overnight at 4 °C. Slides were subsequently washed for 3 × 5 min with PBS before applying secondary antibody (donkey anti-mouse Alexa Fluor 488, Thermo Fisher, A21202, 1:500 dilution) and DAPI (Sigma). Slides were then washed for 3 × 5 min with PBST and then PBS. Finally, samples were prepared for imaging using ProLong Glass Antifade Mountant (Invitrogen). Samples were imaged on a Keyence All-in-One BZ-X Series Fluorescence Microscope, with a ×60 objective, 1× zoom, 1-µm depth resolution and 1,920 × 1,440 *xy* pixel resolution.

Macaque heart sections were received from the NIA. For staining and imaging, slides were first rehydrated using the following steps: 2 × 10 min with Xylene, 100% ethanol, 95% ethanol (in deionized water), 70% ethanol and 50% ethanol before rinsing with deionized water. Slides were subsequently immersed in PBS with 0.5% Triton X-100 for 30 min and incubated with DAPI (Sigma) for 30 min, before 3 × 5 min washes with PBST and 3 × 5 min with PBS. Slides were prepared using ProLong Glass Antifade Mountant (Invitrogen) and imaged as described for mouse heart sections.

Fly nuclear morphology and intensity analysis

For 2D analysis of nuclear morphology, 3D stack images were acquired of the A2–A3 region of the heart as described above (Immunofluorescence and Imaging). The A2–A3 heart region possesses 3–4 CM pairs and therefore 6–8 total CM nuclei. Using ImageJ, CM nuclei were cropped from the larger heart image, within a 22.17 µm^2 / 224 pixel^2 box with the minimal number of z slices to eliminate out-of-plane nuclei from the cuticle or ventral muscle overlaying the CM nucleus. The cropped nuclei were then segmented in FIJI by the macro included in the supplementary software file.

The results were saved and analyzed in Excel. To calculate the aspect ratio the minor axis was divided by the major axis and to calculate the circularity the Excel function '=(4 × PI() × C2) / D2^2' was used. The data were presented and the appropriate statistical tests were performed in Prism.

For 3D analysis of nuclear morphology, the FIJI 3D Mesh plugin[85] was used on the LamC channel of the cropped nuclei stacks. The parameters for seeding and expanding the mesh were as follows: γ, 200.0; pressure, 0.06; image weight, 0.05; β, 0.0; α, 1.0; steric neighbors, 0.0; and divisions, 3.0. Volume and surface area from exported results were copied to Prism for graphing and statistical testing.

The CTNF was calculated using ImageJ. Cropped nuclear stacks, a binary image of the Lamin channel and max projection image were generated as described above. A region of interest (ROI) was generated from the binary image and overlaid onto the max projection image and area and integrated density were measured for the Lamin channel. The relevant macro is included in a supplementary software file.

Subsequently, to account for changes in nuclear size, the background is subtracted relative the area. A clear region outside the nucleus was selected from the Lamin channel and the mean intensity was measured. Then, the following equation was used to calculate the approximate protein amount: CTNF = integrated density − (mean intensity × nuclear area).

Lamin localization

A custom Python code[86] was modified to assess the intensity of Lamin at radially increasing distances from the center of the nucleus to the periphery for the max projected images also generated for nuclear morphology and intensity analysis (Extended Data Fig. 2F). The average mean intensity measurement at periphery was then divided by the average mean intensity the center to obtain the fold enrichment of Lamin at the periphery.

Sarcomere organization

Using ImageJ and confocal stack images of actinin-stained hearts, the dorsal region of the A2–A3 region was projected to isolate a planar

region of sarcomeres and eliminate actinin-stained sarcomeres from the ventral side of the CMs and ventral muscle. ROIs with a single layer of sarcomeres uninterrupted by non-CM cells were then cropped and saved. The isolated actinin regions from the A2–A3 region were then batch processed using a published MatLab code[53] that uses a scanning Fourier transform to calculate organizational index. The input parameters included a sarcomere length of 2.5–3.2 µm, a sarcomere directionality of 90°, a scanning resolution of 16 and at the appropriate pixel-to-µm ratio.

Lifespan assay

To determine lifespan, virgin females were collected and up to 30 flies were separated into each vial. The flies were maintained at 25 °C and transferred to fresh food every 2–3 d, when dead flies were also counted.

Live heart imaging

Hearts were dissected as previously described[52] and heart function was assessed using high-speed digital imaging (142 f.p.s., 9300 EM-CCD cameras, Hamamatsu), a ×10 water-immersion lens and HCImageLive software (Hamamatsu). Using semi-automatic optical heartbeat analysis software (SOHA)[87], fractional shortening (FS) was calculated from the end diastolic diameter (EDD) and end systolic diameters (ESD) by (FS = EDD − ESD / EDD).

Nuclear extraction

Overall, 30–60 dissected hearts were removed from their cuticle and transferred to 1 ml of ice-cold Nuclei EZ lysis buffer (Sigma-Aldrich Nuclei EZ Prep isolation kit) in a 1 ml glass douncer. Twenty loose strokes followed by 10 min on ice and then 15 tight strokes aided dissociation of nuclei from the hearts. The solution was transferred to a low-bind Eppendorf tube and centrifuged at 500*g* for 5 min. The supernatant was removed, the nuclear pellet was resuspended in fresh ice-cold Nuclei EZ lysis buffer and incubated on ice for 5 min. Spinning, removal of supernatant, resuspension and incubation on ice was repeated once more. The samples were centrifuged again at 500*g* before removing the supernatant and resuspending the pellet in PBS for nuclear AFM or Nuclei EZ storage buffer for ATAC-seq.

Atomic force microscopy

For AFM, isolated nuclei in PBS were spun (500*g*, 3 min) onto 12-mm coverslips coated with poly-D-lysine (1 µg µl^{-1} was used to coat coverslips for 5 min, then rinsed with purified water and left to dry overnight). Coverslips were transferred to a glass slide, secured with vacuum grease and covered in a PBS droplet for AFM. Indentation experiments were performed on an MFP-3D Bio Atomic Force Microscope (Oxford Instruments) mounted in a Ti-U fluorescent inverted scope (Nikon Instruments) and used Asylum Research 13, Igor Pro 6.34A software. Nanoworld PNP-TR tips were calibrated for their spring constant using the thermal noise method and used for probing isolated nuclei. A trigger force of 2 nN, an approach velocity constant of at 2 µm s^{-1} and a force distance of 6 µm were used to generate a force map with 12 points across 2 µm^2. Hand4.2-Gal4 was used to drive expression of GFP and thus only GFP-positive nuclei were selected for indentation. The software was used to calculate the Young's modulus using the Hertz equation[88]. Any poor fits to the indentation curve were excluded. Then, the average Young's modulus was calculated from the force map.

Bulk RNA-seq

For gene expression analysis, corresponding adult flies were dissected as previously described[52] to expose the heart. Fat cells were carefully removed from either side of the length of the heart. A minimum of 15 hearts were then pulled from the cuticle using fine forceps and pooled together in Eppendorf tubes containing 300 µl of Qiazol lysis reagent. Hearts were mechanically homogenized using a handheld tissue homogenizer and plastic pestles. Afterward, a further 400 µl of Qiazol lysis reagent was added and the tube flash-frozen in liquid nitrogen. Samples were stored for up to 2 weeks at −80 °C until RNA extraction was performed. Total RNA was then extracted and purified using the QIAGEN miRNeasy Mini kit (cat. no. 217004) as per the protocol. The purified RNA was then processed by the Institute for Genomic Medicine at University California San Diego. RNA integrity was analyzed using an Agilent Tape station system and precise RNA concentration determined using a Qubit 2.0 Fluorometer. Libraries were built using the Illumina TruSeq Stranded RNA High-Throughput Library Prep kit and sequenced on a NovaSeq 6000 for samples with RNA integrity numbers at 9.0 and above.

RNA-seq data were analyzed using Rosalind (https://rosalind.onramp.bio/), with a HyperScale architecture developed by Rosalind. Reads were trimmed using cutadapt[89]. Quality scores were assessed using FastQC[90]. Reads were aligned to the *D. melanogaster* genome build dm6 using STAR[91]. Individual sample reads were quantified using HTseq[92] and normalized via relative log expression using the DESeq2 R library[93]. Read Distribution percentages, violin plots, identity heat maps and sample multidimensional scaling (MDS) plots were generated as part of the quality control step using RSeQC[94]. DEseq2 was also used to calculate fold changes and *P* values and perform optional covariate correction. Clustering of genes for the final heat map of DEGs was performed using the partitioning around medoids method using the fpc R library[95]. Hypergeometric distribution was used to analyze the enrichment of pathways, GO, domain structure and other ontologies. The topGO R library[96,] was used to determine local similarities and dependencies between GO terms to perform Elim pruning correction. Several database sources were referenced for enrichment analysis, including Interpro[97], NCBI[98] MSigDB[99,100], REACTOME[101] and WikiPathways[102]. Enrichment was calculated relative to a set of background genes relevant for the experiment. Panther was used to assess GO terms for gene lists generated in Rosalind.

Hybridization chain reaction

Hearts were dissected as previously described[52] to expose the heart in a 2.5-mm dish. The hearts were relaxed with 10 mM EGTA in oxygenated hemolymph and fixed with 4% formaldehyde in 0.1% Tween 20, PBS for 20 min. Next, the hearts were washed for 2 × 5 min with 0.1% Tween 20, PBS. Then on ice, hearts were incubated each for 5 min with 25%, 50%, 75%, 100%, 75%, 50% and finally 25% methanol in PBS. Hearts were then permeabilized for 2 h at room temperature with 1% PBST. A second fixation was repeated at room temperature and samples were washed for 2 × 5 min with 0.1% Tween, PBS on ice. Then, a 50% 0.1% Tween 20, PBS; 50% 5× SSCT (20× SSC, 10% Tween 20 and ultrapure water) solution was used to wash the samples for 5 min on ice and replaced by 5× SSCT for a further 5 min. The cuticle with the heart attached was then trimmed down to a small rectangle and carefully transferred to a 96-well plate well (each containing a maximum of seven hearts). Within the well, the hearts were incubated with probe hybridization buffer (Molecular Instruments) on ice for 5 min, then the plate was transferred to 37 °C for 30 min. Then, 2 µl of each probe (Molecular Instruments) was prepared in 200 µl of probe hybridization buffer and incubated overnight with the hearts at 37 °C. The following day, samples were washed for 4 × 15 min with probe wash buffer (Molecular Instruments), twice with 5× SSCT and 1 × 5 min with amplification buffer (Molecular Instruments). To prepare the hairpins for fluorescence amplification, 2 µl of corresponding h1 and h2 were heated to 95 °C for 90 s and cooled in the dark for 30 min. The cooled hairpins were then added to 100 µl of amplification buffer and incubated with the hearts overnight at room temperature in the dark. On the next day, while maintained in the dark, samples were washed for 2 × 5 min with 5× SSCT; 2 × 30 min with 5× SSCT; 1 × 5 min with 5× SSCT and finally rinsed 3× with PBS. DAPI (1:250 dilution) was added with the first 5× SSCT 30-min wash or stained subsequently for 15 min in PBST, followed by 3 × 10-min PBST washes

and 3× PBS rinses. Samples were prepared and imaged as described above (Immunofluorescence and Imaging).

To quantify RNA expression levels, processed hearts were imaged as described as above and then imported into ImageJ. For Hand, Tinman and H15 quantification, the A2–A3 heart region confocal stack was converted to a max projection, duplicated and then binarized. Using the max projected image as a guide, the cytoplasmic pockets surrounding the CM nuclei were then then traced and the ROI copied to the binary imaged for particle analysis. As the segmentation was imperfect for transcripts very close together and to account for differences in pocket size, the percentage area covered by the transcripts was used to assess statistical significance in Prism (GraphPad).

As LamC and LamB are expressed in cells other than the CM nuclei (ventral muscle nuclei and cuticle), the narrowest stacks were taken around the nuclear-cytoplasmic pocket to eliminate interfering non-CM transcripts and then the same analysis was conducted as for H15, Tinman and H15. The macro is included in the supplementary software file.

Bulk ATAC-seq

ATAC-seq was performed on 2,000–5,000 nuclei per sample as outlined elsewhere. Samples were permeabilized in cold nuclear permeabilization buffer (0.2% IGEPAL-CA630 (I8896, Sigma), 1 mM dithiothreitol (D9779, Sigma), protease inhibitor (05056489001, Roche) and 5% BSA (A7906, Sigma) in PBS (10010-23, Thermo Fisher Scientific)) for 5 min on a rotator at 4 °C followed by centrifugation for 5 min at 500*g* at 4 °C. After decanting the supernatant, the pellet was resuspended in cold tagmentation buffer (33 mM Tris-acetate, pH 7.8 (BP-152, Thermo Fisher Scientific), 66 mM K-acetate (P5708, Sigma), 11 mM Mg-acetate (M2545, Sigma) and 16% DMF (DX1730, EMD Millipore) in molecular biology grade water (46000-CM, Corning)) followed by incubation with tagmentation enzyme (FC-121-1030; Illumina) at 37 °C with shaking for 30 min. Tagmented DNA was purified using a MinElute PCR purification kit (28004, QIAGEN). The resulting libraries were amplified using NEBNext High-Fidelity 2× PCR Master Mix (M0541, NEB) with primer extension at 72 °C for 5 min, denaturation at 98 °C for 30 s, followed by eight cycles of denaturation at 98 °C for 10 s, annealing at 63 °C for 30 s and extension at 72 °C for 60 s. After purification of amplified libraries using a MinElute PCR purification kit (28004, QIAGEN), double-sided size selection was performed using SPRIselect beads (B23317, Beckman Coulter) with 0.55× beads and 1.5× to sample volume.

Sample processing from FASTQ

FASTQ files were submitted through the UCSD Epigenetics ATAC-seq pipeline (https://github.com/epigen-UCSD/atac_seq_pipeline), based on the ENCODE pipeline. Briefly, reads were aligned using bowtie2, converted to uncompressed BAM files, sorted and index using: bowtie2-X2000–mm–local –1 $fastq1 –2 $fastq2 | samtools view -Su /dev/stdin | samtools sort AND index >xxx.PE2SE.bam &.bai 2> align.log. Poorly mapped (<30 mapping score), duplicate, multimapped and mitochondrial reads were removed using samtools and picard. Tn5 adaptors were removed by truncating + end reads by 4 bp and − end reads by 5 bp and then written to final output BAMs.

Computational analysis was conducted as described by Whitehead et al.[103] and is summarized as follows: BAM files were downloaded from UCSD Center for Epigenomics, sorted and indexed with samtools. Peak calling was performed using MACS2 using the following commands: call peak -f BAMPE -g dm–q 0.01–nomodel–shift –100–extsize 200–keep-dup all. MACS.xls output files and sorted BAMs were used to construct a Diffbind 3.0.9 sample sheet for each comparison: 1-week-old versus 5-week-old w^{1118} samples, wild-type versus LamB iR *attp40* samples and wild-type versus LamC iR *attp2* samples. Samples were read into R Studio using dba(), count densities per peak were calculated using dba.count(), filtering out peaks with <1 read per sample and a summit width of 100 (as recommended by the Diffbind3 vignette). Differential accessibility was calculated using the EdgeR wrapper of dba.analyze(). BED files were generated for each comparison using dba.report() and annotated using HOMER annotatePeaks.pl. Regions were filtered based on a $\log_2$FC of 0.32 and FDR ≤ 0.1. Common features between comparisons were isolated using dplyr's inner_join function of the 'Nearest.Refseq' column output of HOMER. Plots were generated using ggplot2 and ggrepel packages. Panther was used to assess GO terms for gene lists.

Quantitative PCR for monkey and mouse left ventricle

Total RNA was isolated from mouse and monkey frozen left ventricle sections by first grinding frozen tissue in a pestle and mortar with liquid nitrogen to ensure that samples did not degrade. Ground tissue was transferred to an Eppendorf tube and resuspended in 600 µl of RLT lysis buffer from the RNeasy mini RNA extraction kit (QIAGEN). The suspension was then transferred to a QIAshredder column and centrifuged at <10,000*g* for 5 min for further homogenization. The supernatant was collected and total RNA was extracted using the RNAeasy mini RNA extraction kit (QIAGEN) as per the protocol. RNA quality was assessed using an Agilent Tape station system. Poly(A)$^+$ RNA was reverse transcribed using oligo(dT) reagent of the SuperScript IV First-Strand Synthesis kit (Thermo Fisher) and cDNA library generated using manufacturers protocol with a final RNase step. RT–qPCR was then performed in triplicate for each sample using SYBR Green PCR Master mix (Thermo Fisher) and the CFX96 hardware (Bio-Rad). Each gene of interest was normalized to three housekeeping genes[104,105] using the Δ CT equation $2^{-(\text{AvgCqGOI} - \text{AvgCqHK})}$. Primer sequences are shown in Supplementary Table 10 and validated for specificity by melt temperature and efficiency by DNA concentration titration are shown below.

Statistics and reproducibility

Microsoft Excel 2011, MatLab 2020a, Python and Prism 9 software were used to present data and conduct statistical analysis. The respective statistical tests and *n* values are described in the figure legends. For nuclear morphology and intensity analysis and HCR, 6–8 nuclei were cropped from the A2–A3 heart section and a minimum of seven hearts were assessed. For RNA extraction, 15 hearts were collected per condition and at least three biological replicates were acquired. For nuclear extraction, 30–50 hearts were extracted per condition and 3–5 replicates were obtained. For SOHA live heart imaging, >13 hearts were imaged and analyzed. For actinin organization, >14 hearts were analyzed. For lifespan assays, more than 100 flies were recorded. The following statistical significance cutoff was applied: NS $P > 0.05$, $^*P < 0.05$, $^{**}P < 0.01$, $^{***}P < 0.01$, $^{****}P < 0.0001$. No tests were conducted to measure statistical power or normality of distributions. Data were only excluded if they met the criteria of the ROUT method for identifying one or more outliers with a Q of 1%, conducted in GraphPad Prism. Neither the experiments or analysis were randomized or blinded.

Reporting summary

Further information on research design is available in the Nature Portfolio Reporting Summary linked to this article.

Data availability

RNA-seq and ATAC-seq data are deposited at Gene Omnibus Express accession codes GSE185967 and GSE185923, respectively. Source data files are provided and all supporting data from this study are available from the corresponding author upon reasonable request.

Code availability

Software to image fly hearts, analyze their contraction and create kymographs (SOHA) is available at http://sohasoftware.com/index.html. Python code to assess lamin distribution is available at http://englea52.github.io/Englerlab/. Any ImageJ macros have been included in the supplementary software file.

References

1. Phillip, J. M., Aifuwa, I., Walston, J. & Wirtz, D. The mechanobiology of aging. *Annu. Rev. Biomed. Eng.* **17**, 113–141 (2015).
2. Gilbert, H. T. J. & Swift, J. The consequences of ageing, progeroid syndromes and cellular senescence on mechanotransduction and the nucleus. *Exp. Cell. Res.* **378**, 98–103 (2019).
3. Centers for Disease Control and Prevention. *Underlying Cause of Death 1999–2020*. https://wonder.cdc.gov/wonder/help/ucd.html (2022).
4. Sessions, A. O. et al. Extracellular matrix downregulation in the *Drosophila* heart preserves contractile function and improves lifespan. *Matrix Biol.* **62**, 15–27 (2017).
5. Kaushik, G. et al. Vinculin network-mediated cytoskeletal remodeling regulates contractile function in the aging heart. *Sci. Transl. Med.* **7**, 292ra99 (2015).
6. Sessions, A. O. & Engler, A. J. Mechanical regulation of cardiac aging in model systems. *Circ. Res.* **118**, 1553–1562 (2016).
7. Birks, E. J. Molecular changes after left ventricular assist device support for heart failure. *Circ. Res.* **113**, 777–791 (2013).
8. Van Berlo, J. H. et al. C-kit^{+} cells minimally contribute cardiomyocytes to the heart. *Nature* **509**, 337–341 (2014).
9. Cho, S., Irianto, J. & Discher, D. E. Mechanosensing by the nucleus: from pathways to scaling relationships. *J. Cell Biol.* **216**, 305–315 (2017).
10. Janota, C. S., Calero-Cuenca, F. J. & Gomes, E. R. The role of the cell nucleus in mechanotransduction. *Curr. Opin. Cell Biol.* **63**, 204–211 (2020).
11. Saucerman, J. J., Tan, P. M., Buchholz, K. S., McCulloch, A. D. & Omens, J. H. Mechanical regulation of gene expression in cardiac myocytes and fibroblasts. *Nat. Rev. Cardiol.* **16**, 361–378 (2019).
12. Khatau, S. B. et al. A perinuclear actin cap regulates nuclear shape. *Proc. Natl Acad. Sci. USA* **106**, 19017–19022 (2009).
13. Ramdas, N. M. & Shivashankar, G. V. Cytoskeletal control of nuclear morphology and chromatin organization. *J. Mol. Biol.* **427**, 695–706 (2015).
14. Stephens, A. D., Banigan, E. J., Adam, S. A., Goldman, R. D. & Marko, J. F. Chromatin and lamin A determine two different mechanical response regimes of the cell nucleus. *Mol. Biol. Cell.* **28**, 1984–1996 (2017).
15. Stephens, A. D. et al. Chromatin histone modifications and rigidity affect nuclear morphology independent of lamins. *Mol. Biol. Cell.* **29**, 220–233 (2018).
16. van Steensel, B. & Belmont, A. S. Lamina-associated domains: links with chromosome architecture, heterochromatin, and gene repression. *Cell* **169**, 780–791 (2017).
17. Dahl, K. N., Ribeiro, A. J. & Lammerding, J. Nuclear shape, mechanics, and mechanotransduction. *Circ. Res.* **102**, 1307–1318 (2008).
18. Chatzifrangkeskou, M., Kah, D., Lange, J. R., Goldmann, W. H. & Muchir, A. Mutated lamin A modulates stiffness in muscle cells. *Biochem. Biophys. Res. Commun*. https://doi.org/10.1016/j.bbrc.2020.05.102 (2020).
19. Verstraeten, V. L. R. M., Ji, J. Y., Cummings, K. S., Lee, R. T. & Lammerding, J. Increased mechanosensitivity and nuclear stiffness in Hutchinson–Gilford progeria cells: effects of farnesyltransferase inhibitors. *Aging Cell* **7**, 383–393 (2008).
20. Lammerding, J. et al. Lamins A and C but not lamin B1 regulate nuclear mechanics. *J. Biol. Chem.* **281**, 25768–25780 (2006).
21. Srivastava, L.K., Ju, Z., Ghagre, A. & Ehrlicher, A. J. Spatial distribution of lamin A/C determines nuclear stiffness and stress-mediated deformation. *J. Cell Sci.* **134**, jcs248559 (2021).
22. Buxboim, A. et al. Matrix elasticity regulates lamin-A,C phosphorylation and turnover with feedback to actomyosin. *Curr. Biol.* **24**, 1909–1917 (2014).
23. Dahl, K. N. et al. Distinct structural and mechanical properties of the nuclear lamina in Hutchinson–Gilford progeria syndrome. *Proc. Natl Acad. Sci. USA* **103**, 10271–10276 (2006).
24. Brandt, A. et al. Developmental control of nuclear size and shape by kugelkern and kurzkern. *Curr. Biol.* **16**, 543–552 (2006).
25. Jevtić, P. et al. Concentration-dependent effects of nuclear lamins on nuclear size in Xenopus and mammalian cells. *J. Biol. Chem.* **290**, 27557–27571 (2015).
26. Pajerowski, J. D., Dahl, K. N., Zhong, F. L., Sammak, P. J. & Discher, D. E. Physical plasticity of the nucleus in stem cell differentiation. *Proc. Natl Acad. Sci. USA* **104**, 15619–15624 (2007).
27. Bonne, G. et al. Mutations in the gene encoding lamin A/C cause autosomal dominant Emery-Dreifuss muscular dystrophy. *Nat. Genet.* **21**, 285–288 (1999).
28. Di Barletta, M. R. et al. Different mutations in the LMNA gene cause autosomal dominant autosomal recessive Emery-Dreifuss muscular dystrophy. *Am. J. Hum. Genet.* **66**, 1407–1412 (2000).
29. Taylor, M. R. G. et al. Natural history of dilated cardiomyopathy due to lamin A/C gene mutations. *J. Am. Coll. Cardiol.* **41**, 771–780 (2003).
30. Capell, B. C., Collins, F. S. & Nabel, E. G. Mechanisms of cardiovascular disease in accelerated aging syndromes. *Circ. Res.* **101**, 13–26 (2007).
31. Scaffidi, P. & Misteli, T. Reversal of the cellular phenotype in the premature aging disease Hutchinson–Gilford progeria syndrome. *Nat. Med.* **11**, 440–445 (2005).
32. Liu, B. et al. Genomic instability in laminopathy-based premature aging. *Nat. Med.* **11**, 780–785 (2005).
33. Goldman, R. D. et al. Accumulation of mutant lamin A progressive changes in nuclear architecture in Hutchinson–Gilford progeria syndrome. *Proc. Natl Acad. Sci. USA* **101**, 8963–8968 (2004).
34. Shumaker, D. K. et al. Mutant nuclear lamin A leads to progressive alterations of epigenetic control in premature aging. *Proc. Natl Acad. Sci. USA* **103**, 8703 (2006).
35. Haithcock, E. et al. Age-related changes of nuclear architecture in *Caenorhabditis elegans*. *Proc. Natl Acad. Sci. USA* **102**, 16690–16695 (2005).
36. Brandt, A., Krohne, G. & Großhans, J. The farnesylated nuclear proteins kugelkern and lamin B promote aging-like phenotypes in *Drosophila* flies. *Aging Cell* **7**, 541–551 (2008).
37. Scaffidi, P. & Misteli, T. Lamin A-dependent nuclear defects in human aging. *Science* **312**, 1059–1063 (2006).
38. Larson, K. et al. Heterochromatin formation promotes longevity and represses ribosomal RNA synthesis. *PLoS Genet*. https://doi.org/10.1371/journal.pgen.1002473 (2012).
39. McClintock, D. et al. The mutant form of lamin a that causes Hutchinson-Gilford progeria is a biomarker of cellular aging in human skin. *PLoS ONE* **2**, e1269 (2007).
40. Messner, M. et al. Upregulation of the aging related LMNA splice variant progerin in dilated cardiomyopathy. *PLoS ONE* **13**, e0196739 (2018).
41. Afilalo, J. et al. Age-related changes in lamin A/C expression in cardiomyocytes. *Am. J. Physiol. Circ. Physiol.* **293**, H1451–H1456 (2007).
42. Freund, A., Laberge, R. M., Demaria, M. & Campisi, J. Lamin B1 loss is a senescence-associated biomarker. *Mol. Biol. Cell* **23**, 2066–2075 (2012).
43. Chen, H., Zheng, X. & Zheng, Y. Age-associated loss of lamin-B leads to systemic inflammation and gut hyperplasia. *Cell* **159**, 829–843 (2014).
44. Han, L. et al. Lamin B2 levels regulate polyploidization of cardiomyocyte nuclei and myocardial regeneration. *Dev. Cell* https://doi.org/10.1016/j.devcel.2020.01.030 (2020).

45. Nikolova, V. et al. Defects in nuclear structure and function promote dilated cardiomyopathy in lamin A/C-deficient mice. *J. Clin. Invest.* **113**, 357–369 (2004).
46. Cammarato, A. et al. A mighty small heart: the cardiac proteome of adult *Drosophila melanogaster*. *PLoS ONE* **6**, e18497 (2011).
47. Nishimura, M. et al. A dual role for integrin-linked kinase and β1-integrin in modulating cardiac aging. *Aging Cell* **13**, 431–440 (2014).
48. Choi, H. M. T. et al. Third-generation in situ hybridization chain reaction: Multiplexed, quantitative, sensitive, versatile, robust. *Development* **145**, 1–10 (2018).
49. bin Imtiaz, M. K. et al. Declining lamin B1 expression mediates age-dependent decreases of hippocampal stem cell activity. *Cell Stem Cell* **28**, 967–977 (2021).
50. Li, H. et al. Fly Cell Atlas: a single-nucleus transcriptomic atlas of the adult fruit fly. *Science* https://doi.org/10.1126/science.abk2432 (2022).
51. Prakash, A. et al. Cardiac abnormalities in patients with Hutchinson–Gilford progeria syndrome. *JAMA Cardiol.* **3**, 326–334 (2018).
52. Vogler, G. & Ocorr, K. Visualizing the beating heart in *Drosophila*. *J. Vis. Exp.* https://doi.org/10.3791/1425 (2009).
53. Salick, M. R. et al. The scanning gradient Fourier transform (SGFT) method for assessing sarcomere organization and alignment. *J. Appl. Phys.* **127**, 194701 (2020).
54. Cheedipudi Sirisha, M. et al. Genomic reorganization of lamin-associated domains in cardiac myocytes is associated with differential gene expression and DNA methylation in human dilated cardiomyopathy. *Circ. Res.* **124**, 1198–1213 (2019).
55. Buenrostro, J. D., Giresi, P. G., Zaba, L. C., Chang, H. Y. & Greenleaf, W. J. Transposition of native chromatin for fast and sensitive epigenomic profiling of open chromatin, DNA-binding proteins and nucleosome position. *Nat. Methods* **10**, 1213–1218 (2013).
56. Davidson, E. H. & Erwin, D. H. Gene regulatory networks and the evolution of animal body plans. *Science* **311**, 796–800 (2006).
57. Schulze, S. R. et al. Molecular genetic analysis of the nested *Drosophila melanogaster* lamin C gene. *Genetics* **171**, 185–196 (2005).
58. Brand, A. H. & Perrimon, N. Targeted gene expression as a means of altering cell fates and generating dominant phenotypes. *Development* **118**, 401–415 (1993).
59. McGee, M. D. et al. Loss of intestinal nuclei and intestinal integrity in aging *C. elegans*. *Aging Cell* **10**, 699–710 (2011).
60. Zhao, M. et al. Segmentation and classification of two-channel *C. elegans* nucleus-labeled fluorescence images. *BMC Bioinformatics* https://doi.org/10.1186/s12859-017-1817-3 (2017).
61. Dreesen, O. et al. Lamin B1 fluctuations have differential effects on cellular proliferation and senescence. *J. Cell Biol.* **200**, 605–617 (2013).
62. Schulze, S. R. et al. A comparative study of *Drosophila* and human A-type lamins. *PLoS ONE* https://doi.org/10.1371/journal.pone.0007564 (2009).
63. Cosgrove, B. D. et al. Nuclear envelope wrinkling predicts mesenchymal progenitor cell mechano-response in 2D and 3D microenvironments. *Biomaterials* **270**, 120662 (2021).
64. Nava, M. M. et al. Heterochromatin-driven nuclear softening protects the genome against mechanical stress-induced damage. *Cell* **181**, 800–817 (2020).
65. Shah, P. et al. Pathogenic LMNA variants disrupt cardiac lamina-chromatin interactions and de-repress alternative fate genes. *Cell Stem Cell* **28**, 938–954.e9 (2021).
66. Zheng, X. et al. Lamins organize the global three-dimensional genome from the nuclear periphery. *Mol. Cell* **71**, 802–815 (2018).
67. Hu, B. et al. Plant lamin-like proteins mediate chromatin tethering at the nuclear periphery. *Genome Biol.* **20**, 1–18 (2019).
68. Ulianov, S. V. et al. Nuclear lamina integrity is required for proper spatial organization of chromatin in *Drosophila*. *Nat. Commun.* **10**, 1176 (2019).
69. Sawh, A. N. et al. Lamina-dependent stretching and unconventional chromosome compartments in early *C. elegans* embryos. *Mol. Cell* **78**, 96–111 (2020).
70. Chang, L. et al. Nuclear peripheral chromatin-lamin B1 interaction is required for global integrity of chromatin architecture and dynamics in human cells. *Protein Cell* https://doi.org/10.1007/s13238-020-00794-8 (2020).
71. Noguchi, A. et al. Decreased lamin B1 levels affect gene positioning and expression in postmitotic neurons. *Neurosci. Res.* https://doi.org/10.1016/j.neures.2021.05.011 (2021).
72. Li, C.-L. et al. Region-specific H3K9me3 gain in aged somatic tissues in *Caenorhabditis elegans*. *PLoS Genet.* **17**, e1009432 (2021).
73. Pickersgill, H. et al. Characterization of the *Drosophila melanogaster* genome at the nuclear lamina. *Nat. Genet.* **38**, 1005–1014 (2006).
74. van Bemmel, J. G. et al. The insulator protein SU(HW) fine-tunes nuclear lamina interactions of the *Drosophila* genome. *PLoS ONE* https://doi.org/10.1371/journal.pone.0015013 (2010).
75. Han, Z. & Olson, E. N. Hand is a direct target of Tinman and GATA factors during *Drosophila* cardiogenesis and hematopoiesis. *Development* **132**, 3525–3536 (2005).
76. Bodyak, N. Gene expression profiling of the aging mouse cardiac myocytes. *Nucleic Acids Res.* **30**, 3788–3794 (2002).
77. Shen, T. et al. Tbx20 regulates a genetic program essential to adult mouse cardiomyocyte function. *J. Clin. Invest.* **121**, 4640–4654 (2011).
78. Sakabe, N. J. et al. Dual transcriptional activator and repressor roles of TBX20 regulate adult cardiac structure and function. *Hum. Mol. Genet.* **21**, 2194–2204 (2012).
79. Stennard, F. A. et al. Murine T-box transcription factor Tbx20 acts as a repressor during heart development, and is essential for adult heart integrity, function and adaptation. *Development* **132**, 2451–2462 (2005).
80. Akazawa, H. & Komuro, I. Roles of cardiac transcription factors in cardiac hypertrophy. *Circ. Res.* **92**, 1079–1088 (2003).
81. Thattaliyath, B. D., Livi, C. B., Steinhelper, M. E., Toney, G. M. & Firulli, A. B. HAND1 and HAND2 are expressed in the adult-rodent heart and are modulated during cardiac hypertrophy. *Biochem. Biophys. Res. Commun.* **297**, 870–875 (2002).
82. Natarajan, A. et al. Human eHAND, but not dHAND, is down-regulated in cardiomyopathies. *J. Mol. Cell. Cardiol.* **33**, 1607–1614 (2001).
83. Bigot, A. et al. Replicative aging down-regulates the myogenic regulatory factors in human myoblasts. *Biol. Cell* **100**, 189–199 (2008).
84. Musarò, A. et al. Enhanced expression of myogenic regulatory genes in aging skeletal muscle. *Exp. Cell. Res.* **221**, 241–248 (1995).
85. Smith, M. B., Chaigne, A. & Paluch, E. K. An active contour ImageJ plugin to monitor daughter cell size in 3D during cytokinesis. *Methods Cell. Biol.* **137**, 323–340 (2017).
86. Beri, P. et al. Cell adhesiveness serves as a biophysical marker for metastatic potential. *Cancer Res.* https://doi.org/10.1158/0008-5472.CAN-19-1794 (2019).
87. Ocorr, K., Fink, M., Cammarato, A., Bernstein, S. & Bodmer, R. Semi-automated optical heartbeat analysis of small hearts. *J. Vis. Exp.* https://doi.org/10.3791/1435 (2009).
88. Hertz, H. Ueber den kontakt elastischer koerper. *J. fuer die Reine Angew. Math.* **92**, 156 (1881).
89. Martin, M. Cutadapt removes adapter sequences from high-throughput sequencing reads. *EMBnet J.* **17**, 10–12 (2011).

90. Babraham Bioinformatics. *FastQC a quality control tool for high throughput sequence data*. https://www.bioinformatics.babraham.ac.uk/projects/fastqc/ (2019).
91. Dobin, A. et al. STAR: ultrafast universal RNA-seq aligner. *Bioinformatics* **29**, 15–21 (2013).
92. S, A., PT, P. & W, H. HTSeq: a Python framework to work with high-throughput sequencing data. *Bioinformatics* **31**, 166–169 (2015).
93. Love, M. I., Huber, W. & Anders, S. Moderated estimation of fold change and dispersion for RNA-seq data with DESeq2. *Genome Biol.* **15**, 1–21 (2014).
94. L, W., S, W. & W, L. RSeQC: quality control of RNA-seq experiments. *Bioinformatics* **28**, 2184–2185 (2012).
95. Hennig, C. *fpc: Flexible Procedures for Clustering* https://cran.r-project.org/web/packages/fpc/index.html (2020).
96. Alexa, A. & Rahnenfuhrer, J. *topGO: Enrichment Analysis for Gene Ontology*. R package version 2.50.0. https://bioconductor.org/packages/release/bioc/html/topGO.html (2022).
97. Mitchell, A. L. et al. InterPro in 2019: improving coverage, classification and access to protein sequence annotations. *Nucleic Acids Res.* **47**, D351–D360 (2019).
98. LY, G. et al. The NCBI BioSystems database. *Nucleic Acids Res.* https://doi.org/10.1093/nar/gkp858 (2010).
99. Subramanian, A. et al. Gene set enrichment analysis: a knowledge-based approach for interpreting genome-wide expression profiles. *Proc. Natl Acad. Sci. USA* **102**, 15545–15550 (2005).
100. Liberzon, A. et al. Molecular signatures database (MSigDB) 3.0. *Bioinformatics* **27**, 1739 (2011).
101. A, F. et al. The Reactome Pathway Knowledgebase. *Nucleic Acids Res.* **46**, D649–D655 (2018).
102. DN, S. et al. WikiPathways: a multifaceted pathway database bridging metabolomics to other omics research. *Nucleic Acids Res.* **46**, D661–D667 (2018).
103. Whitehead, A. J., Hocker, J. D., Ren, B. & Engler, A. J. Improved epicardial cardiac fibroblast generation from iPSCs. *J. Mol. Cell. Cardiol.* **164**, 58–68 (2022).
104. Ahn, K. et al. Selection of internal reference genes for SYBR green qRT–PCR studies of rhesus monkey (*Macaca mulatta*) tissues. *BMC Mol. Biol.* **9**, 1–8 (2008).
105. Ruiz-Villalba, A. et al. Reference genes for gene expression studies in the mouse heart. *Sci. Rep.* **7**, 1–9 (2017).

Acknowledgements

The authors thank K. Jepsen of the Institute for Genomic Medicine (UCSD) for technical assistance with sequencing; E. Molina (Sanford Consortium Stem Cell Core) for access and maintenance of the LSM780 microscope; K. Christman, R. Middleton, J. Tuler and K. Birmingham (UCSD) for use and dissection of hearts from the aged mouse model; N. Varki and S. Choudhury of the Mouse Phenotyping Core (UCSD) for assistance with histological preparations; and UCSD undergraduate students S. Skalak, M. Naguib, I. Madan, J. Yun and S. Sharma for assistance with fly husbandry and immunostaining experiments. We thank the Bloomington Drosophila Stock Center (P40OD018537), R. Bodmer, K. Ocorr, J. Grosshans and L. Walrath for providing fly strains. The authors acknowledge funding and equipment support from the NIH (R01AG045428 to A.J.E. and S10OD026929 to UCSD IGM Genomics Center) as well as intramural support from the NIA (to E.G.L. and M.W.). Fellowship support was provided by the American Heart Association (20POST35180048 to N.J.K.), the National Science Foundation (to A.J.W. and P.B.), the ARCS Foundation (to A.J.W.) and the NIH (T32GM008666 to J.D.H.). Work at the Center for Epigenomics was supported in part by the UCSD School of Medicine.

Author contributions

N.J.K., R.B. and A.J.E. conceived the project and designed experiments. N.J.K. and S.H.S. performed experiments. B.H. and G.V. developed the HCR protocol for adult fly hearts. N.J.K. analyzed experimental data. P.B. developed the Python Lamin distribution analysis pipeline. N.J.K., A.J.W. and J.D.H. performed ATAC-seq and analyzed sequencing data. B.R. oversaw ATAC-seq assay design and provided technical expertise. G.V. oversaw and provided technical expertise for fly imaging and HCR experiments. M.W. performed macaque husbandry and isolated macaque tissue. E.G.L. managed the macaque colony. The manuscript was written by N.J.K., R.B. and A.J.E. with input from the other authors.

Competing interests

The authors declare no competing interests.

Additional information

Extended data is available for this paper at https://doi.org/10.1038/s43587-022-00323-8.

Supplementary information The online version contains supplementary material available at https://doi.org/10.1038/s43587-022-00323-8.

Correspondence and requests for materials should be addressed to Adam J. Engler.

Peer review information *Nature Aging* thanks the anonymous reviewers for their contribution to the peer review of this work.

https://doi.org/10.1038/s43587-022-00323-8

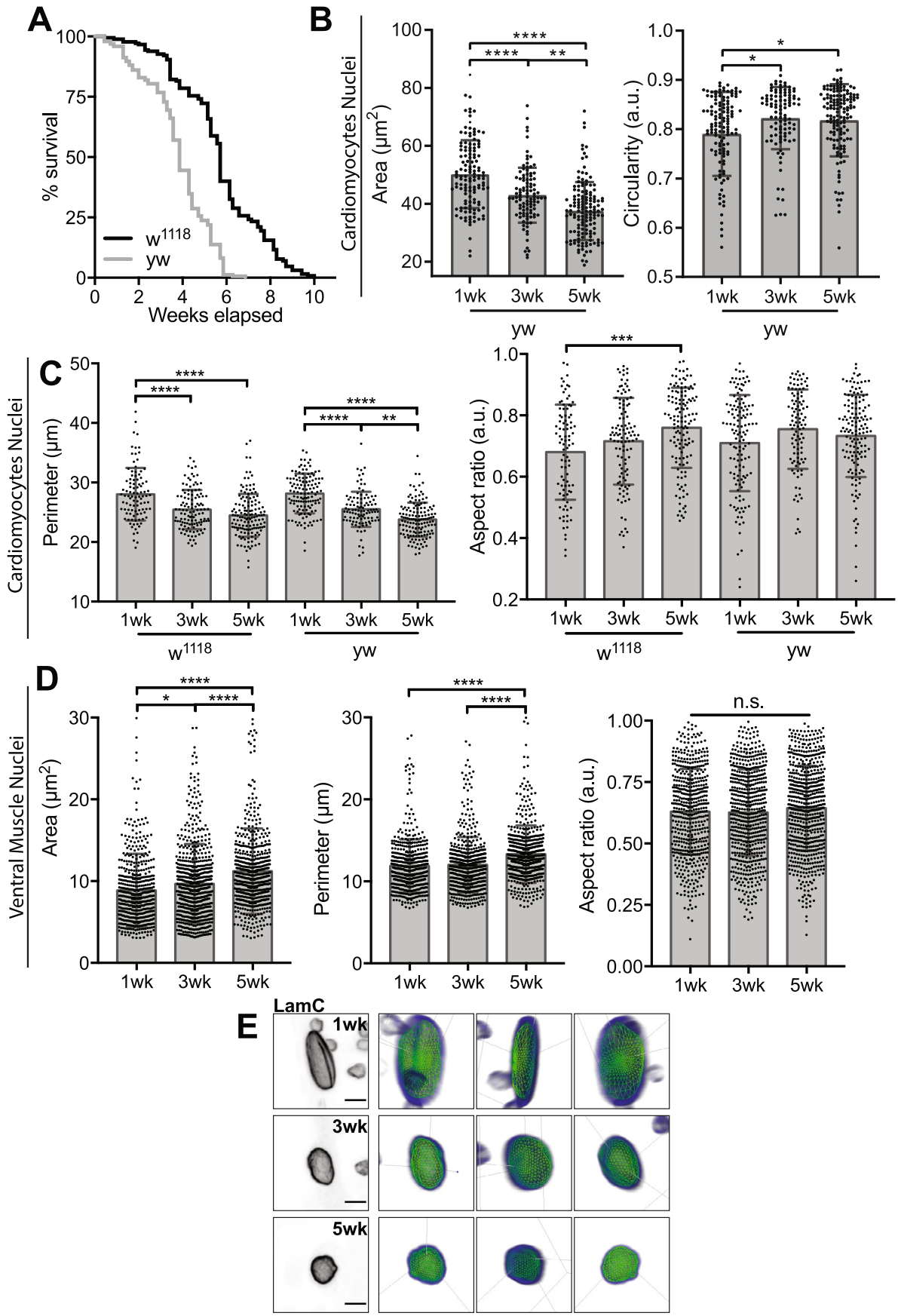

Extended Data Fig. 1 | See next page for caption.

https://doi.org/10.1038/s43587-022-00323-8

Extended Data Fig. 1 | Nuclear Dynamics in Cardiac and Skeletal Muscle Cells. (A) Kaplan–Meier survival curve for *yw* (gray) and w^{1118} (black) flies. n = 103 and flies, respectively, were used in the plot. $p < 10^{-3}$ based on Log-Rank (Mantel-Cox) test between the two strains. **(B)** Plots of 2D projected area (left) and circularity data (right) for *yw* flies. n = 129, 108, and 143 for *yw* flies at 1-, 3-, and 5 weeks, respectively. **(C)** Cardiomyocyte nuclear area (left) and aspect ratio (right) plotted for w^{1118} and *yw* flies as a function of adult age. n = 96, 116, and 141 nuclei for for w^{1118} flies and n = 129, 108, and 143 for *yw* flies at 1-, 3-, and 5 weeks of adulthood, respectively. **(D)** Ventral muscle nuclear area (left), perimeter (center), and aspect ratio (right) from w^{1118} flies at 1-, 3-, and 5 weeks of adulthood. n = 528, 604, 661 ventral muscle nuclei from w^{1118} flies at 1-, 3-, and 5 weeks of adulthood. **(E)** Representative images of the 3D wireframe mesh of cardiomyocyte nuclei from w^{1118} flies at 1- (top), 3- (middle), and 5 weeks (bottom) of adulthood. Scale bar is 5 µm. *$p < 0.05$, **$p < 10^{-2}$, ***$p < 10^{-3}$, and ****$p < 10^{-4}$ by one-way ANOVA with Tukey multiple comparisons test. Error bars in all graphs refer to mean + /- SD.

https://doi.org/10.1038/s43587-022-00323-8

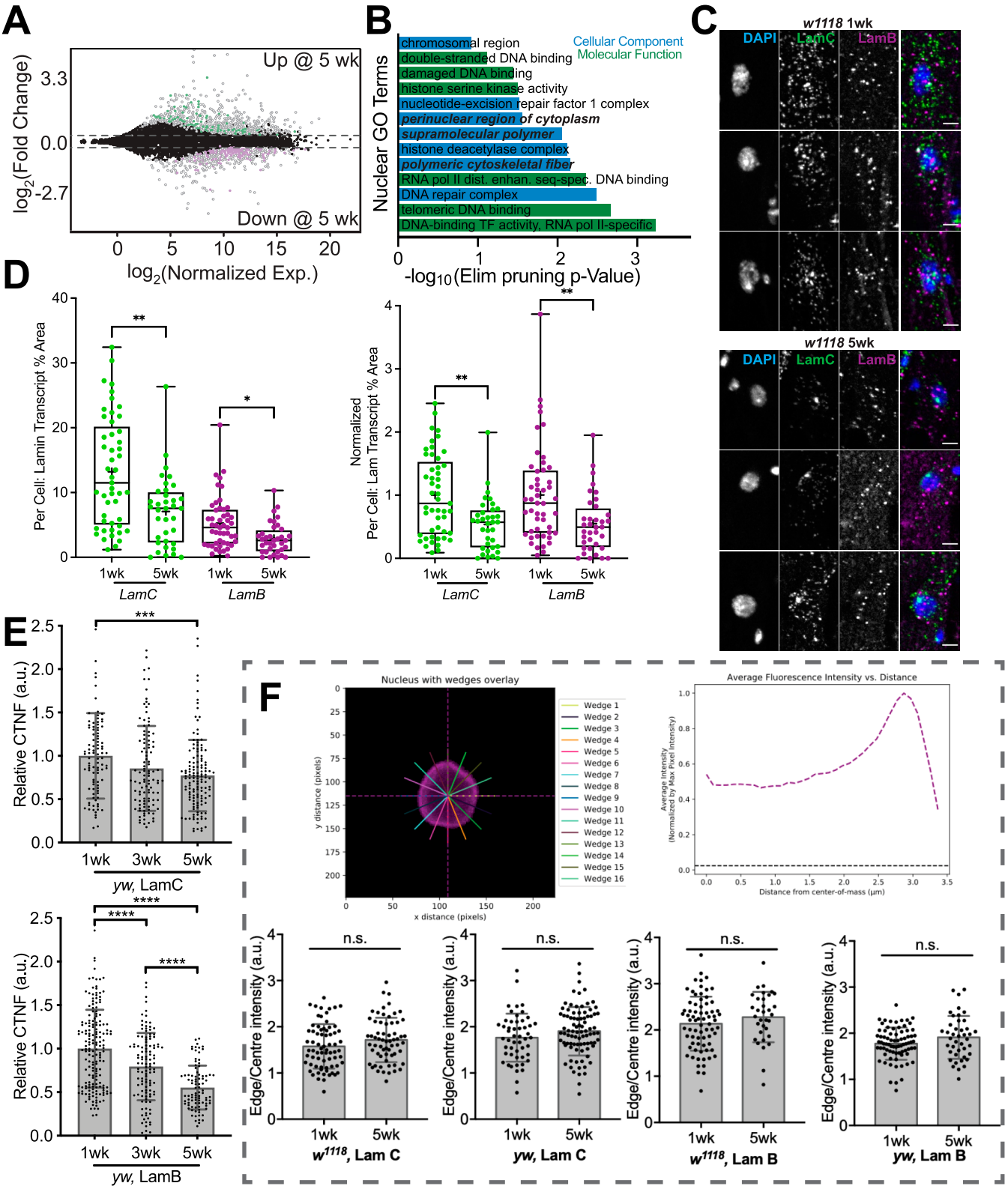

Extended Data Fig. 2 | See next page for caption.

https://doi.org/10.1038/s43587-022-00323-8

Extended Data Fig. 2 | Natural Aging Downregulates LamC and LamB but does not affect their localization. (A) MA plot of all genes from 1- and 5-week adult w^{1118} fly hearts showing $\log_2$ fold change (FC) and mean normalized expression counts. Data is shown in black for genes −1.25 < FC < 1.25 (dashed lines) or p-adj > 0.05. Open circles represent genes that do not map to a nuclear ontological term. Green and purple data represent DEGs that are up- or downregulated in 5-week adult flies, respectively. **(B)** Cellular component and molecular function ontological terms for genes associated with the nuclear envelope GO term, organized by their elimination pruning p-value. **(C)** Representative images of 1 and 5 week w^{1118} fly heart nuclei stained for DNA, and LamC (green) and LamB (purple) mRNA transcripts. Scale bar, 5 µm. **(D)** Left plot shows area percentage occupied by mRNA transcripts per cardiomyocyte in 1- and 5-week-old adult w^{1118} fly hearts. Right plot normalizes data to mean area at 1 week for each transcript. n = 49, 36, 49, and 36 nuclei from w^{1118} flies at 1 and 5 weeks for *LamC* and *LamB*, respectively. **(E)** Corrected total nuclear fluorescence (CTNF) of 1, 3, and 5 week *yw* flies for *LamC* (top) and *LamB* (bottom). n = 94, 106, and 133 nuclei for *LamC* and n = 173, 115, and 90 nuclei for *LamB* for 1, 3, and 5 week adults, respectively. **(F)** Image showing a representative nucleus with multiple lines radiating out from its centroid (left) to create line plots that are averaged into a single radial profile of the fluorescent intensity (right). Lower panel, the ratio of edge to center intensity is plotted. n = 72, 63, 73, and 33 nuclei from w^{1118} flies at 1 and 5 weeks for *LamC* and *LamB*, respectively. n = 51, 87, 77, and 42 nuclei from *yw* flies at 1 and 5 weeks for *LamC* and *LamB*, respectively. *p < 0.05, **p < 10^{-2}, ***p < 10^{-3}, and ****p < 10^{-4} by one-way ANOVA with Tukey multiple comparisons test. Bars in (D) refer to min to max, with median and 25th and 75th interquartile range and error bars in (E-F) refer to mean + /- SD.

https://doi.org/10.1038/s43587-022-00323-8

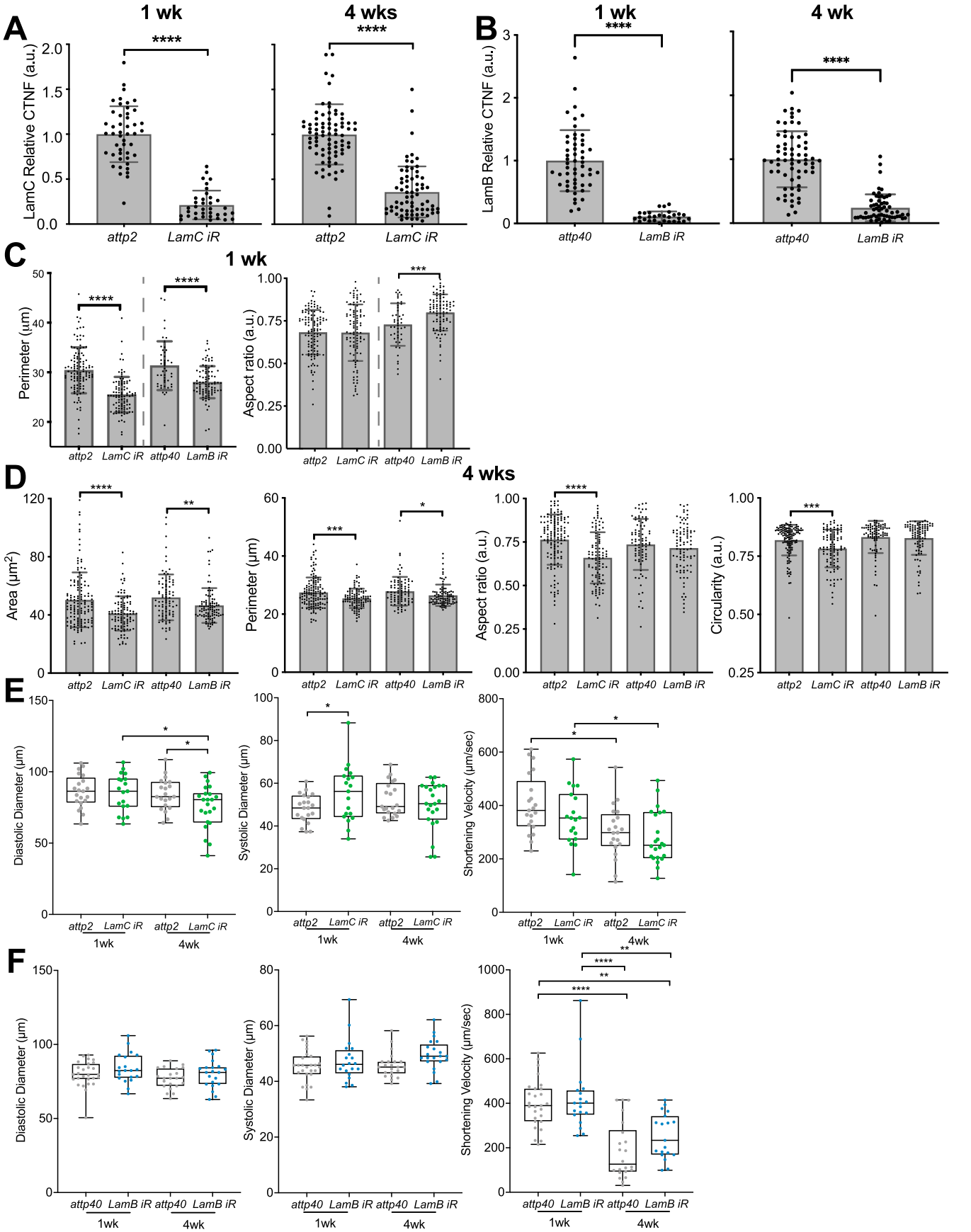

Extended Data Fig. 3 | See next page for caption.

https://doi.org/10.1038/s43587-022-00323-8

Extended Data Fig. 3 | Validation and Morphological and Functional Characterization of LamB and LamC RNAi lines. Corrected total nuclear fluorescence (CTNF) for cardiomyocytes from **(A)** *LamC* RNAi and **(B)** *LamB* RNAi fly lines and their respective controls, that is, *attp2* and *attp40*, n = 47, 36, 79, and 69 nuclei from *attp2* and *LamC* RNAi flies at 1 and 4 weeks (left to right). n = 53, 29, 65, and 61 nuclei from *attp40* and *LamB* RNAi flies at 1 and 4 weeks (left to right). **(C)** Plots quantifying nuclear perimeter (left, n = 111, 96, 46, and 89 nuclei/condition) and aspect ratio (right, n = 113, 97, 46, and 92 nuclei/condition) for *LamB*, *LamC* RNAi and their genetic controls. **(D)** Plots quantifying nuclear area, perimeter, aspect ratio, and circularity (left to right) for *LamB* and *LamC* RNAi lines and their genetic control background at 4 weeks. For all plots, n = 136, 101, 86, and 95 nuclei/condition left to right. **(E-F)** Plots of diastolic and systolic diameters, and shortening velocity determined from SOHA imaging for *attp2* control and *LamC RNAi* flies **(E)**, and *attp40* control and *LamB RNAi* flies **(F)** at 1 and 4 weeks. Each *LamC RNAi* plots, n = 21, 23, 25, and 27 nuclei/condition, left to right. Each *LamB RNAi* plots, n = 31, 21, 26, and 25 nuclei/condition, left to right. For panels A-D, *$p < 0.05$, **$p < 10^{-2}$, ***$p < 10^{-3}$, and ****$p < 10^{-4}$ from a two-sided unpaired t-test at each time point and RNAi line. For E-F, *$p < 0.05$, **$p < 10^{-2}$, ***$p < 10^{-3}$, and ****$p < 10^{-4}$ by one-way ANOVA with Tukey multiple comparisons test. Error bars in (A-D) refer to mean + /- SD, and bars in (E, F) refer to min to max, with median and 25th and 75th interquartile range.

https://doi.org/10.1038/s43587-022-00323-8

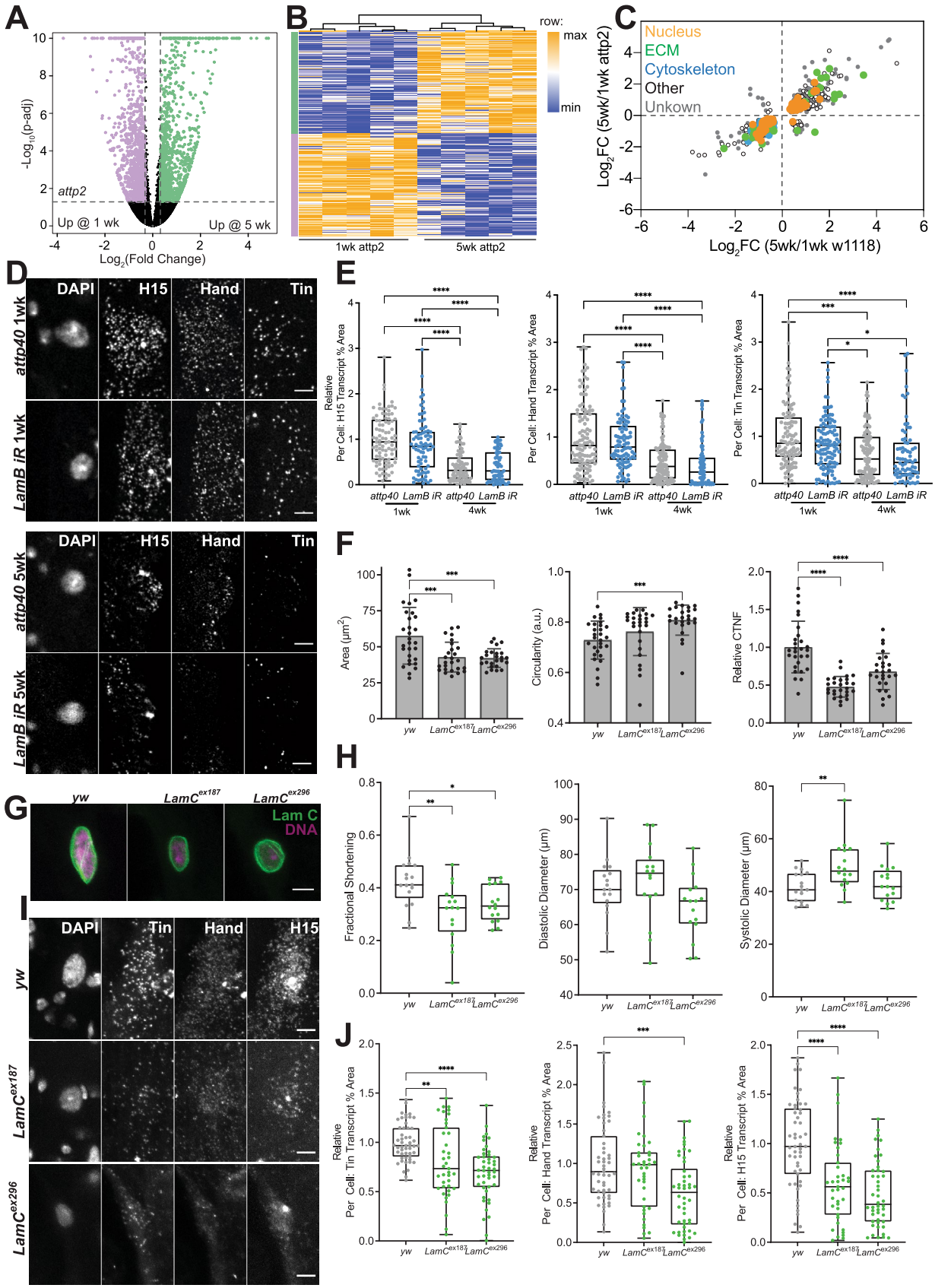

Extended Data Fig. 4 | See next page for caption.

https://doi.org/10.1038/s43587-022-00323-8

Extended Data Fig. 4 | Validation of transgenic fly background, effects of LamB on myogenic transcription factor expression, and LamC heterozygous flies. (A) Volcano plot and **(B)** heat map of bulk RNA-seq from surgically dissected *attp2* heart tubes. Fold change represents 5-week *attp2* fly hearts normalized to 1-week-old hearts and p-adj was computed from quintuplicate. 1,998 differentially expressed genes (DEGs) were assessed from cutoffs of $-0.32 > \log_2(FC) > 0.32$ (or $-1.25 > FC > 1.25$) (dashed lines) from comparisons of 15 fly hearts per replicate; DEGs increasing and decreasing with age are shown in green and purple, respectively. Heat map columns were hierarchically clustered using Euclidean distance and linkage shown by the dendrogram. Heat maps are normalized within each gene/row. **(C)** 635 of 688 genes were co-regulated DEGs (92.3%) in the w^{1118} and *attp2* control fly hearts, and plotted based on their fold change with age. DEGs were annotated based on their ontological categorization as nuclear (orange), extracellular matrix (ECM; green), or cytoskeletal (blue). A subset of DEGs either did not fit those categories (black/white) or lacked a known ontology (gray). Only 7.7% of all DEGs were dysregulated. **(D)** Representative images of *attp40* control and *LamB* RNAi flies at 1 and 4 weeks showing *H15*, *Hand* and *Tin* transcription factor mRNA and DAPI. Scale bar is 5 µm. **(E)** Quantification of the per cell percentage area for each transcript in *attp40* control and *LamB* RNAi flies at 1 and 4 weeks. For H15, n = 93, 87, 85, and 71 cells, left to right. For Hand, n = 111, 96, 105, and 76 cells, left to right. For Tin, n = 105, 118, 102, and 76 cells, left to right. **(F)** Quantification of cardiomyocyte nuclear area, circularity and LamC corrected total nuclear fluorescence for 1-week-old female control yw/w^{1118} *and* heterozygous LamC excision mutants $yw/w^{1118};LamC^{ex187}/+$ *and* $yw/w^{1118};LamC^{296}/+$ fly hearts and their representative images in **(G)** showing staining for LamC (green) and DNA (Magenta), scale bare = 5 µm. For **(F)**, n = 29, 26, 25 (CM nuclei, left to right) **(H)** Quantification of heart parameters: fractional shortening, diastolic diameter and systolic diameter for background control and heterozygous LamC excision mutants. n = 17, 16, 16 (heart tubes, left to right) **(I)** Representative images of Hand, H15 and Tin mRNA in heterozygous LamC excision mutants, presented with quantification of per cell percentage area for each transcript in **(J)**. n = 52, 39, 46 (CM nuclei, left to right). $^*p < 0.05$, $^{**}p < 10^{-2}$, $^{***}p < 10^{-3}$, and $^{****}p < 10^{-4}$ by one-way ANOVA with Tukey multiple comparisons test. Box plots in (E, H, J) refer to min to max, with median and 25th and 75th interquartile range and error bars in (F) refer to mean + /- SD.

https://doi.org/10.1038/s43587-022-00323-8

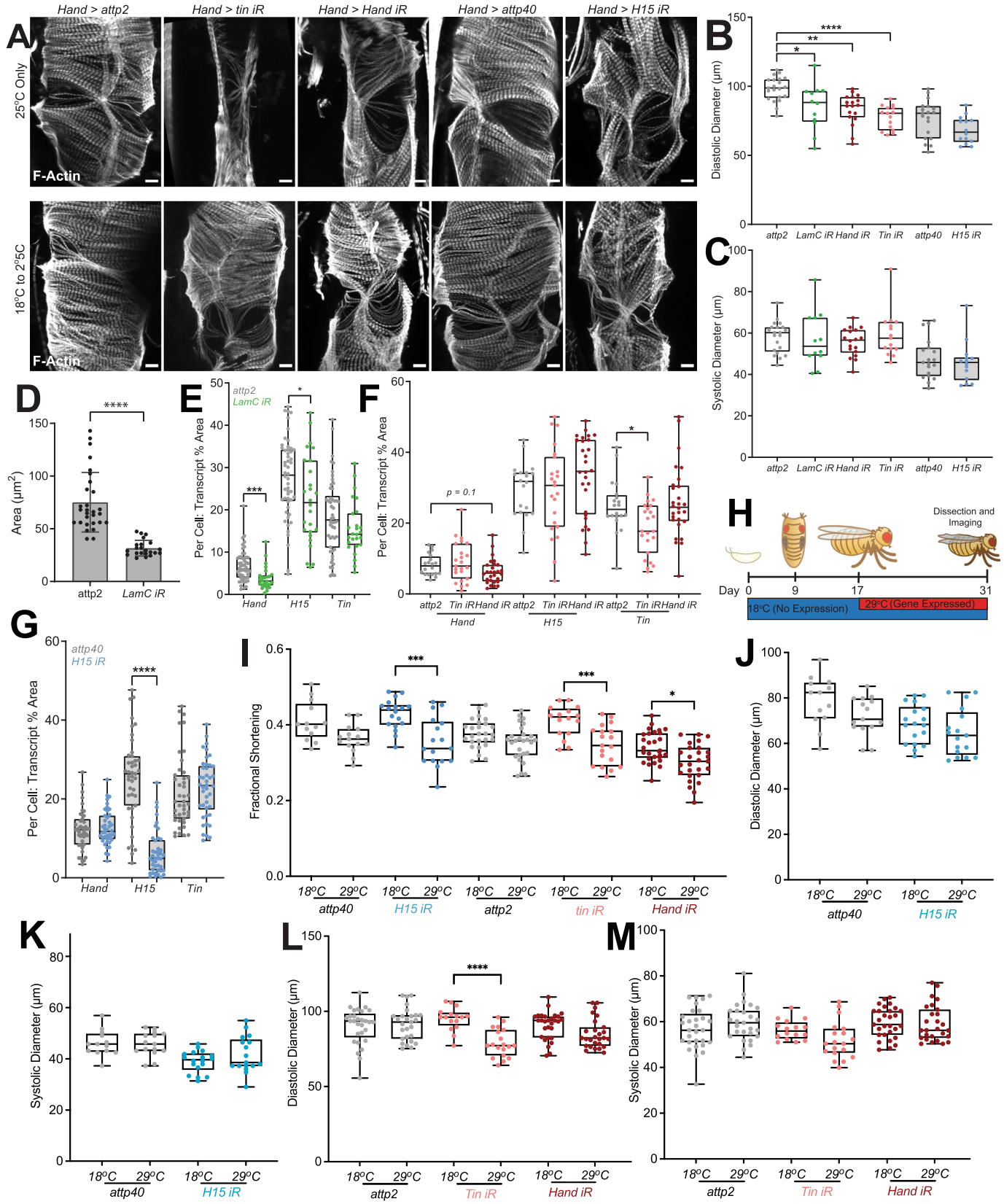

Extended Data Fig. 5 | See next page for caption.

https://doi.org/10.1038/s43587-022-00323-8

Extended Data Fig. 5 | Effects of Adult Myogenic Transcription Factor Loss on of Heart Tube Morphology and Function. (A) Representative images of A2-A3 heart region visualized by phalloidin (F-Actin) with the indicated transgenes expressed under the control of the *Hand-Gal4* promoter. Scale bar is 10 µm. At least three heart tubes were imaged for each condition. **(B)** Diastolic and **(C)** systolic diameters of heart tubes from control fly lines (*attp40* and *attp2*) and their corresponding transgenic flies expressing the indicated RNAi. n = 10, 12, 18, 15, 19 and 14 (heart tubes, left to right). **(D)** CM nuclear area in *attp2* control and *LamC RNAi* hearts subject to regime described in Fig. 6a. n = 29 and 22 (CM Nuclei, left to right). **(E-G)** Quantification of the per cell, percentage area for Hand, H15 and Tin transcripts upon KD of **(E)** *LamC*, **(F)** *Hand* (red), *Tin* (pink) and respective control *attp2* (grey), and **(G)** *H15* (blue) and *attp40* control (grey), induced as in Fig. 6a. n = 32 and 26 (CM Nuclei/genotype) in **(E)**, n = 20, 23, 28 (CM Nuclei/genotype, left to right) in **(F)** and n = 43 and 42 (CM Nuclei/genotype) in **(G)**. **(H)** Schematic of temperature-sensitive transgenic expression where 29 °C enables transgenic expression due to the denaturation of Gal4 transcription factor suppressor, $Gal80^{ts}$. **(I)** Fractional shortening of surgically exposed heart tubes at 18 °C and 29 °C for controls (black), and KD of *tin* (pink), *Hand* (brown), and *H15* (blue) with corresponding diastolic and systolic diameters in **(J-M)**. n = 13, 15, 18, 15, 26, 27, 16, 19, 29, 27, 29, and 21 (heart tubes/transgene/ temperature; left to right as shown in **(I)**). *$p < 0.05$, **$p < 10^{-2}$, ***$p < 10^{-3}$, and ****$p < 10^{-4}$ by independent t-test and one-way ANOVA with Kruskal–Wallis test and Dunn's comparisons test. Box plots show to min to max, with median and 25th and 75th interquartile range and error bars in (D) refer to mean + /- SD.

https://doi.org/10.1038/s43587-022-00323-8

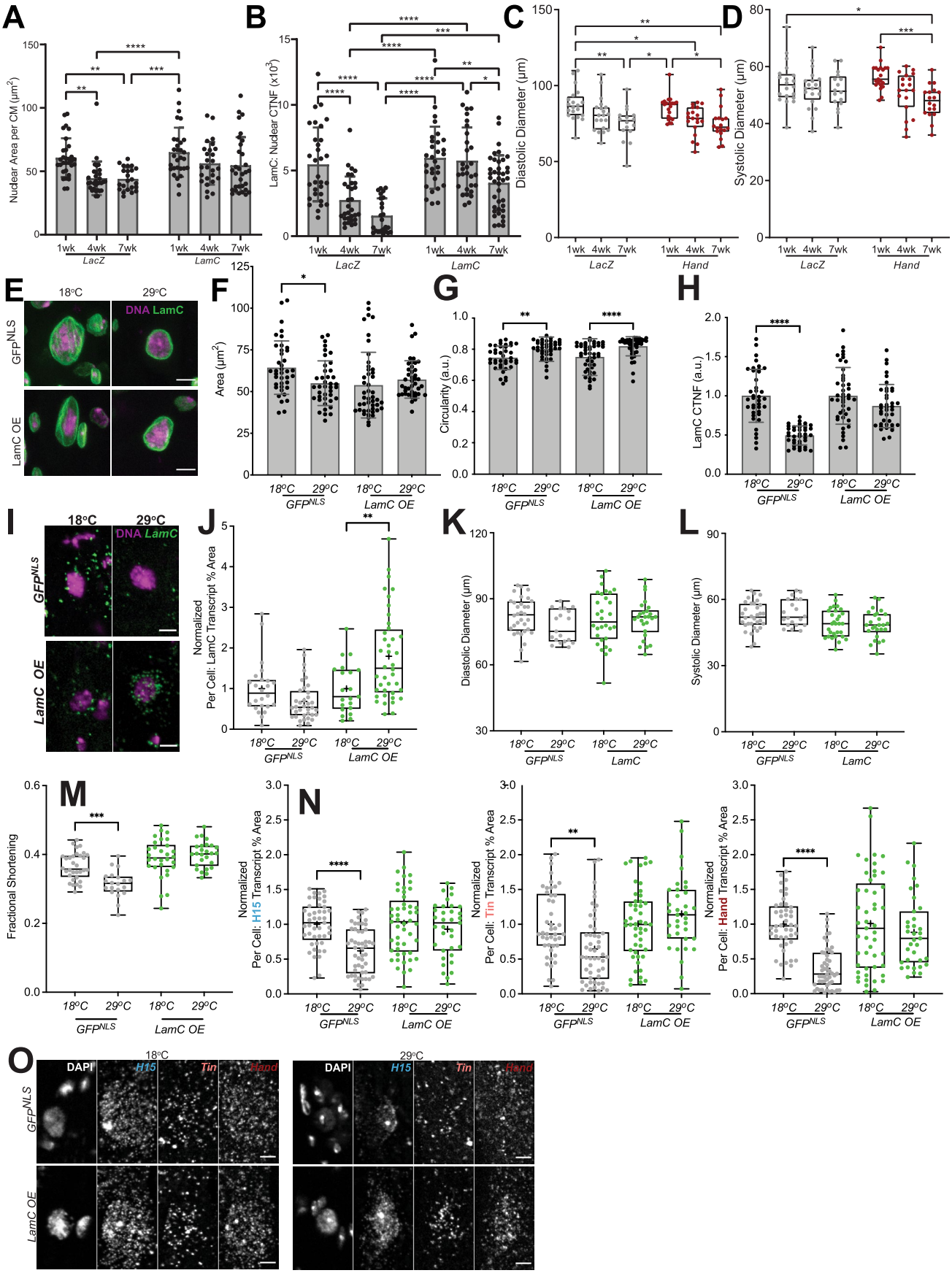

Extended Data Fig. 6 | See next page for caption.

https://doi.org/10.1038/s43587-022-00323-8

Extended Data Fig. 6 | Effects of LamC and Myogenic Transcription Factor Overexpression. For panels A-D and as outlined in Fig. 6a, flies were reared at 18 °C and shifted to 25 °C upon eclosure. Nuclear area **(A)** and CTNF **(B)** for hearts overexpressing LacZ (control) and LamC from 1 to 7 weeks. n = 31, 41, 23, 30, 26, and 31 cells (A, left to right) and n = 31, 31, 24, 29, 30, and 40 cells (B, left to right). **(C)** Diastolic and **(D)** systolic diameters of LacZ and Hand OE flies at 1, 4, and 7 weeks of adulthood. **(E)** Representative images (left) for nuclei from flies at 18 °C and 29 °C expressing GFP^{NLS} transgene or LamC OE from HandGal,$tubGal80^{ts}$;$tubGal80^{ts}$ based upon regime described in S5H. Scale bar is 5 µm. Plots of **(F)** projected nuclear area, **(G)** circularity, and **(H)** and corrected total nuclear fluorescence (CTNF) of LamC protein as a function of temperature and transgene expression. n = 39, 40, 46, and 41 nuclei (left to right). **(I)** For GFP^{NLS} and LamC OE at 18 °C and 29 °C, representative images of LamC mRNA transcripts. Scale bar is 5 µm. **(J)** Quantification of LamC transcript area per CM in GFP^{NLS} and LamC OE hearts, at 18 °C and 29 °C. n = 24, 36, 20 and 40 CMs, left to right. Diastolic **(K)** and systolic **(L)** diameters, and **(M)** fractional shortening for GFP^{NLS} and LamC OE at 18 °C and 29 °C. n = 32, 19, 30 and 26 heart tubes, left to right. **(N)**. A plot for each transcription factor is shown and quantifies the per cell, percentage area for each transcript. For all transcripts, n = 50, 56, 49 and 35 cells, left to right. **(O)** Representative images for tin (pink), Hand (brown), and H15 (blue) transcripts in GFP^{NLS} and LamC OE at 18 °C and 29 °C. Scale bar is 5 µm. *$p < 0.05$, **$p < 10^{-2}$, ***$p < 10^{-3}$, and ****$p < 10^{-4}$ by two-way ANOVA with Sidaks multiple comparisons test (A-D) and one-way ANOVA with Kruskal-Wallis test and Dunn's comparisons test (F-N). Error bars in (A, B, F-H) refer to mean + /- SD and all box plots display min to max, with median and 25^{th} and 75^{th} interquartile range.

https://doi.org/10.1038/s43587-022-00323-8

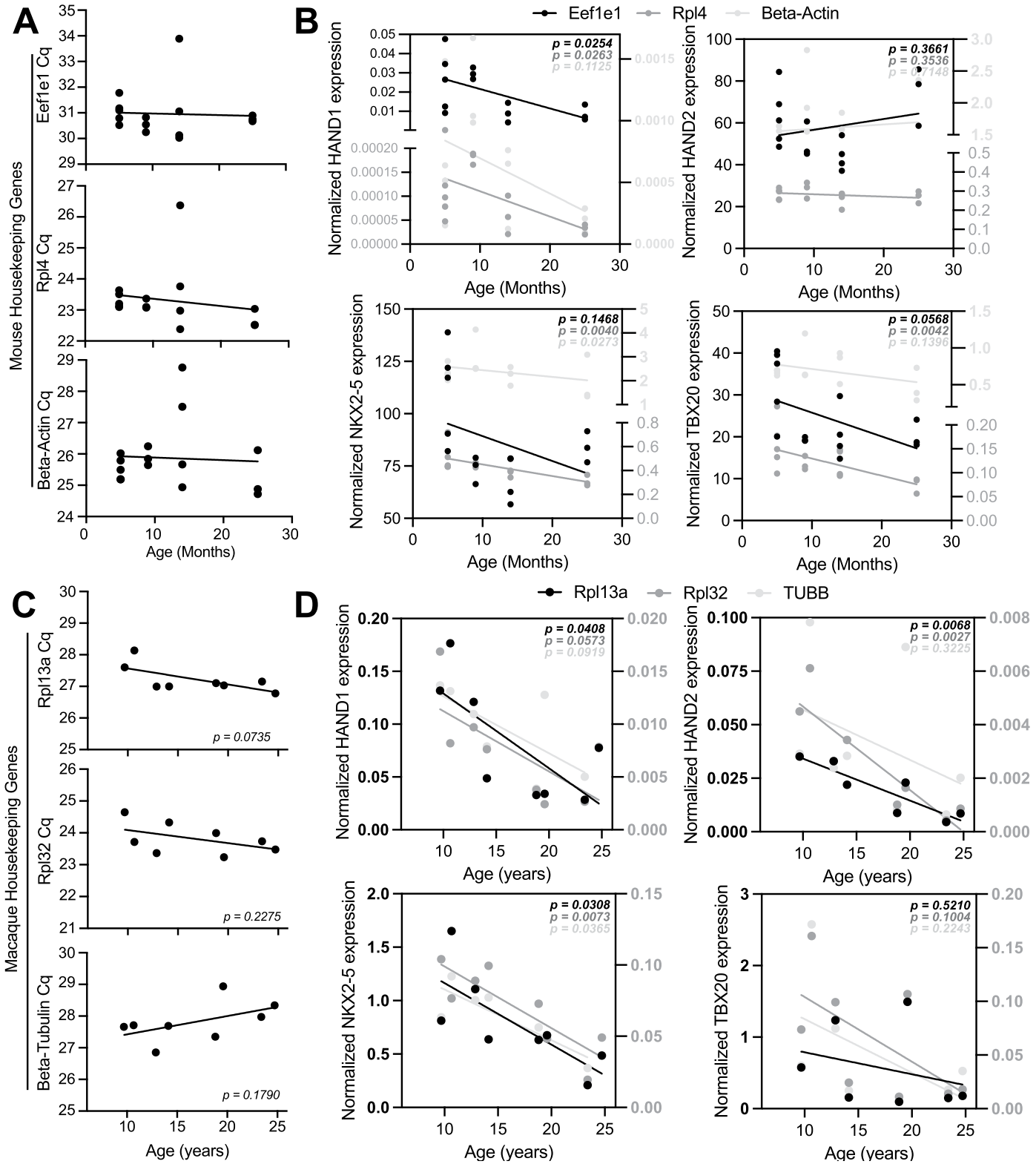

Extended Data Fig. 7 | Myogenic transcription factor expression in the left ventricles of aged nonhuman primates and mice. (A) Expression of three housekeeping genes for mice are plotted as a function of age with a linear and associated p-value shown. Data is plotted for raw Cq values. **(B)** Expression of four transcription factors in mice is shown, normalized to each housekeeper gene. Data normalized to Eef1e1 (black), Rpl4 (medium gray), and ACTB (light gray) are plotted using the left and right y-axes, depending on the axis label colors. P-values for each fit are shown in the upper right corner. **(C)** Expression of three housekeeping genes for rhesus macaques are plotted as a function of age with a linear and associated p-value shown. Data is plotted for raw Cq values. **(D)** Expression of four transcription factors in rhesus macaques is shown, normalized to each housekeeper gene. Data normalized to Rpl13a (black) and TUBB2 (light gray) use the left y-axis whereas Rpl32 uses the right y-axis (medium gray). P-values for each fit are shown in the upper right corner.

nature portfolio

Corresponding author(s): Engler, Adam J.

Last updated by author(s): 10/02/2022

Reporting Summary

Nature Portfolio wishes to improve the reproducibility of the work that we publish. This form provides structure for consistency and transparency in reporting. For further information on Nature Portfolio policies, see our Editorial Policies and the Editorial Policy Checklist.

Statistics

For all statistical analyses, confirm that the following items are present in the figure legend, table legend, main text, or Methods section.

n/a	Confirmed
☐	☒ The exact sample size (*n*) for each experimental group/condition, given as a discrete number and unit of measurement
☐	☒ A statement on whether measurements were taken from distinct samples or whether the same sample was measured repeatedly
☐	☒ The statistical test(s) used AND whether they are one- or two-sided *Only common tests should be described solely by name; describe more complex techniques in the Methods section.*
☒	☐ A description of all covariates tested
☒	☐ A description of any assumptions or corrections, such as tests of normality and adjustment for multiple comparisons
☐	☒ A full description of the statistical parameters including central tendency (e.g. means) or other basic estimates (e.g. regression coefficient) AND variation (e.g. standard deviation) or associated estimates of uncertainty (e.g. confidence intervals)
☐	☒ For null hypothesis testing, the test statistic (e.g. *F*, *t*, *r*) with confidence intervals, effect sizes, degrees of freedom and *P* value noted *Give P values as exact values whenever suitable.*
☒	☐ For Bayesian analysis, information on the choice of priors and Markov chain Monte Carlo settings
☒	☐ For hierarchical and complex designs, identification of the appropriate level for tests and full reporting of outcomes
☒	☐ Estimates of effect sizes (e.g. Cohen's *d*, Pearson's *r*), indicating how they were calculated

Our web collection on statistics for biologists contains articles on many of the points above.

Software and code

Policy information about availability of computer code

Data collection	Python code to assess Lamin distribution is available at http://englea52.github.io/Englerlab/. Any ImageJ macros have been included in Quantification and Statistical Analysis Section in Materials and Methods. Matlab 2020a was used to assess sarcomere organization using published code (Salick, M. R. et al. The scanning gradient Fourier transform (SGFT) method for assessing sarcomere organization and alignment. J. Appl. Phys. 127, 194701 (2020)).
Data analysis	RNA-Sequencing data was analyzed by ROSALIND® (https://rosalind.onramp.bio/). ATAC-sequencing data was analyzed through UCSD's center for epigenetics ATAC-seq pipeline (https://github.com/epigen-UCSD/atac_seq_pipeline). Microsoft Excel 2011, and Prism 9 Software was used for statistical analysis.

For manuscripts utilizing custom algorithms or software that are central to the research but not yet described in published literature, software must be made available to editors and reviewers. We strongly encourage code deposition in a community repository (e.g. GitHub). See the Nature Portfolio guidelines for submitting code & software for further information.

Data

Policy information about availability of data

All manuscripts must include a data availability statement. This statement should provide the following information, where applicable:

- Accession codes, unique identifiers, or web links for publicly available datasets
- A description of any restrictions on data availability
- For clinical datasets or third party data, please ensure that the statement adheres to our policy

RNA-Seq and ATAC-Seq data is deposited at Gene Omnibus Express (GEO) Accession GSE185967 and GSE185923, respectively. All supporting data from this study are available from the corresponding author upon reasonable request.

Field-specific reporting

Please select the one below that is the best fit for your research. If you are not sure, read the appropriate sections before making your selection.

☒ Life sciences ☐ Behavioural & social sciences ☐ Ecological, evolutionary & environmental sciences

For a reference copy of the document with all sections, see nature.com/documents/nr-reporting-summary-flat.pdf

Life sciences study design

All studies must disclose on these points even when the disclosure is negative.

Sample size	No sample size calculation was performed since we planned experiements based on earlier studies form the Rolf Bodmer and Adam Engler laboratories. N numbers were always sufficient to obtain a measurement for a positive control, e.g., a sufficient number of hearts were pooled to measure bulk transcriptome by RNA-seq.
Data exclusions	Data was only excluded if data point was deemed an outlier by the ROUT method with 1% Q, using GraphPad Prism 9.
Replication	Nuclear morphology and intensity, HCR and Sarcomere Organization measurements were assessed from at least 7 heart tubes. Survival experiments were repeated 2-3 times. AFM measurements were obtained at least 3 times on separate days. Sequencing analysis was conducted at least 3 times from at least 15 pooled hearts. Live heart measurements were obtained from at least 13 hearts and in most cases repeated on separate days. Mouse and non-primate heart tissue was assessed across at least three samples.
Randomization	Samples were not randomized, however live heart and lifespan experiments were carried out on separate days, and repeated weeks to months apart to reduce the chance of batch effects.
Blinding	Analyses were not formally blinded, but imaging or dissection of live hearts were often performed by separate individuals. Live heart analysis and nuclear segmentation was performed in batch across genotypes so were in many cases effectively blinded.

Reporting for specific materials, systems and methods

We require information from authors about some types of materials, experimental systems and methods used in many studies. Here, indicate whether each material, system or method listed is relevant to your study. If you are not sure if a list item applies to your research, read the appropriate section before selecting a response.

Materials & experimental systems

n/a	Involved in the study
☐	☒ Antibodies
☒	☐ Eukaryotic cell lines
☒	☐ Palaeontology and archaeology
☐	☒ Animals and other organisms
☒	☐ Human research participants
☒	☐ Clinical data
☒	☐ Dual use research of concern

Methods

n/a	Involved in the study
☒	☐ ChIP-seq
☒	☐ Flow cytometry
☒	☐ MRI-based neuroimaging

Antibodies

Antibodies used	Mouse anti-LamC (DSHB, LC28.26), 1:500. Mouse anti-LamB, 1:100 (DSHB, ADL195). Mouse anti-actinin (DSHB, 2G3-3D7) 1:100. DAPI (Sigma), 1:500. Rhodamine-Phalloidin (ThermoFisher, R415), 1:250. Donkey anti-mouse Alexa Fluor 488 (ThermoFisher, A21202), 1:500. anti-Lamin A/C (Cell Signaling, 4777)
Validation	anti-LamC (DSHB, LC28.26) and anti-LamB, 1:100 (DSHB, ADL195) were verified against their RNAi as shown in Figure 3A. anti-actinin (DSHB, 2G3-3D7) was generated and verified by Saide et al., (doi:10.1083/jcb.109.5.2157) anti-Lamin A/C 4777, Cell Signaling was verified by the company.

Animals and other organisms

Policy information about studies involving animals; ARRIVE guidelines recommended for reporting animal research

Laboratory animals	The following fly lines were used from the Bloomington stock center: white-1118, w1118, yellow-white yw, attp2; UAS-Luciferase (#31603), UAS-LamC RNAi (#31621), attp40 (#36304), UAS-LamB RNAi (#57501), UAS-Stinger-GFP (#84277), UAS-tinman RNAi (#50663), UAS-H15 RNAi (#57415), UAS-Hand RNAi (#28977). Hand4.2Gal4 was acquired from Olsen Laboratory and modified by the Bodmer lab to make Hand4.2Gal4, TubGal80ts; TubGal80ts. UAS-LamC, Lamc187, and LamC296 was gifted by the Wallrath laboratory. Female flies were used for all studies. C57BL/6 male and female mice were used in aging studies (5 x 5 month, 3 x 9

	month, 4 x 14 month and 3 x 24 month). Male Rhesus macaque (no strain) were also used at ages 8.87, 9.7, 10.66, 12.88, 14.12, 18.81, 19.59, 23.39, 24.73, and 25.48 years.
Wild animals	This study did not involve wild animals.
Field-collected samples	This study did not involve collection of animals from the field.
Ethics oversight	All mouse experiments were performed in according to the guidelines established by the Institutional Animal Care and Use Committee at the University of California San Diego. Use of aged C57BL/6 mice was approved by the University of California San Diego Institutional Animal Care and Use Committee under study #S08172. All animals were provided with food and water ad libitum until the specific age time point at which point animals were euthanized by asphyxiation followed by cervical dislocation. Rhesus Macaques were maintained at the NIA in accordance with NIH Institutional Animal Care and Use Committee protocol AG000238-07 (Effects of Aging on Experimental Atherosclerosis in Nonhuman Primates).

Note that full information on the approval of the study protocol must also be provided in the manuscript.